

SMR/208 - 47

SPRING COLLEGE IN MATERIALS SCIENCE

ON

"METALLIC MATERIALS"

(11 May - 19 June 1987)

BACKGROUND MATERIAL FOR LECTURES ON  
"FIELD ION MICROSCOPY OF ALLOYS"

BY

P. HAASEN  
Institut für Metallphysik  
der Universität Göttingen  
Hospitalstr. 3  
D-3400 Göttingen  
Federal Republic of Germany

# APPLICATION OF ANALYTICAL FIELD-ION MICROSCOPY TO THE DECOMPOSITION OF ALLOYS

*P. Haasen*<sup>1</sup>

Department of Materials Science and Engineering, Stanford University,  
Stanford, CA 94305

*R. Wagner*

Institut für Physik, GKSS Forschungszentrum, D2054 Geesthacht, and  
SFB 126 Göttingen-Clausthal, West Germany

## INTRODUCTION

Many technologically important properties of alloys, such as mechanical strength, or the coercivity of ferromagnetic materials, are essentially controlled by the precipitate microstructure that results from the diffusion-controlled decomposition reaction of the originally supersaturated matrix. A fundamental understanding of the thermodynamics, the kinetics, and the mechanism of the phase transformation that leads to well-defined precipitate microstructures is, therefore, of great interest in metallurgy.

The course of a decomposition reaction, including the early stages (during which composition fluctuations and second-phase nuclei are formed) as well as the coarsening stages can generally *not* be followed continuously by any one microanalytical technique. The progress of a decomposition reaction is usually reconstructed from the microstructure that has developed at various stages of the phase transformation. Thus, it is

<sup>1</sup> On leave from Institut für Metallphysik, Universität Göttingen, D34 Göttingen, West Germany.

necessary to analyze the spatial extension and the amplitude of composition fluctuations of incipient, second-phase particles, as well as the morphology, number density, size, and chemical composition of discrete precipitates at various stages of the phase transformation. For this purpose microanalytical tools are required that are capable of resolving very small solute clusters, and simultaneously identifying their chemical composition.

Although the first requirement is frequently met by neutron (SANS) and X-ray (SAXS) small angle scattering techniques, and also by TEM (for particles larger than about 4 nm), the chemical analysis of particles smaller than about 12 nm is usually not possible using any of the standard microanalytical tools, such as the electron microprobe, or scanning transmission electron microscopy combined with an energy-dispersive X-ray analyzer.

This gap in the analysis of ultrafine precipitates can be bridged by employing the atom-probe field-ion microscope (AP FIM) (1), which is a combination of a field-ion microscope (FIM) and a time-of-flight mass spectrometer (atom-probe, AP). This instrument has the unique capability of imaging and identifying single atoms. For more than ten years the AP FIM has been used successfully for chemical analyses of, for example, individual carbide (2-4), or nitride precipitates (5) in various steels, and  $\gamma'$  particles in cast commercial nickel-based superalloys (6), which escaped detection by TEM [for a comprehensive review, see (7)]. These results are not treated again in this review.

The recent development of unified precipitation theories (8, 9), which treat nucleation, growth, and coarsening ("Ostwald ripening") as concurrent processes until precipitation is completed, has stimulated several AP FIM studies of the early stage precipitation kinetics in metastable supersaturated binary or ternary alloys. Some experimental results from those studies and their agreement with theoretical predictions are the subject of the second part of this article; various aspects of the AP FIM analysis of decomposing alloys are covered in the first part.

For many two-phase alloys the important theoretical question remains open of whether the phase transformation is initiated by the *formation of small nuclei* having a composition similar to that of the equilibrium phase (or at least similar to that of the intermediate metastable phase, which is formed in some alloys prior to the formation of the equilibrium phase), or whether it is initiated by *spinodal decomposition*. Since the latter reaction is caused by the thermodynamic instability of the quasi-uniform solid solution within the spinodal range (10-12), the decomposition occurs by the growth of three-dimensional composition waves without any nucleation barrier larger than  $\sim kT$  to be overcome. The wavelengths of these long-range composition fluctuations are initially typically about 5 nm, but will

grow with aging time to tens of nm. According to various theories of spinodal decomposition (10, 11), the amplitudes of the composition waves increase gradually with aging time, starting from almost zero, until they reach a value corresponding to the concentration of the completely precipitated second phase.

The microstructures in the later transformation stages (where some of the conventional microanalytical tools can now be applied) evolve from either classical nucleation or spinodal decomposition, but do not necessarily differ from each other. Therefore, it is usually not accurate to deduce the mode of the initial decomposition reaction simply from observations of the microstructure in later transformation stages. The only way to prove experimentally that a solid solution decomposes spinodally is to show by a suitable microanalytical technique that the composition waves are gradually amplified during aging until discrete precipitates of the second phase have finally emerged.

As discussed in Section 1, in principle, long-range composition fluctuations can be analyzed with the atom-probe FIM, though sometimes statistical problems impede a straightforward interpretation of the measured composition profiles. The technique has been applied to study phase separation in a number of supersaturated alloys that are thought to decompose spinodally. This belief is based on some typical microstructural features (13), which, according to Cahn's phenomenological theory of spinodal decomposition (10), can—but do not necessarily—evolve from a spinodal reaction. Results and conclusions from some of these studies are discussed in Section 2.

## 1. EXPERIMENTAL ASPECTS

### 1.1 Basic Design and Operation of an Atom-Probe FIM

Since Müller and co-workers (18) conceived of and published the first design of an atom-probe FIM, several instruments specially developed for application to various metallurgical problems have been described in the literature (7, 14-17). Currently, about twelve instruments are being operated in metallurgical laboratories worldwide.

Figure 1 shows the basic features and electronic circuitry of an atom-probe FIM designed for the investigation of phase separation in alloys. Essentially, the instrument consists of two parts: the FIM to image the specimen, and the time-of-flight (ToF) spectrometer (the atom-probe) in which single ions, field evaporated from the FIM specimen surface, are identified. The imaging-screen contains in its center a probe-hole of about 2.5 mm in diameter. Field-evaporated ions, originating from the area covered by the projection of the probe-hole onto the specimen surface (the

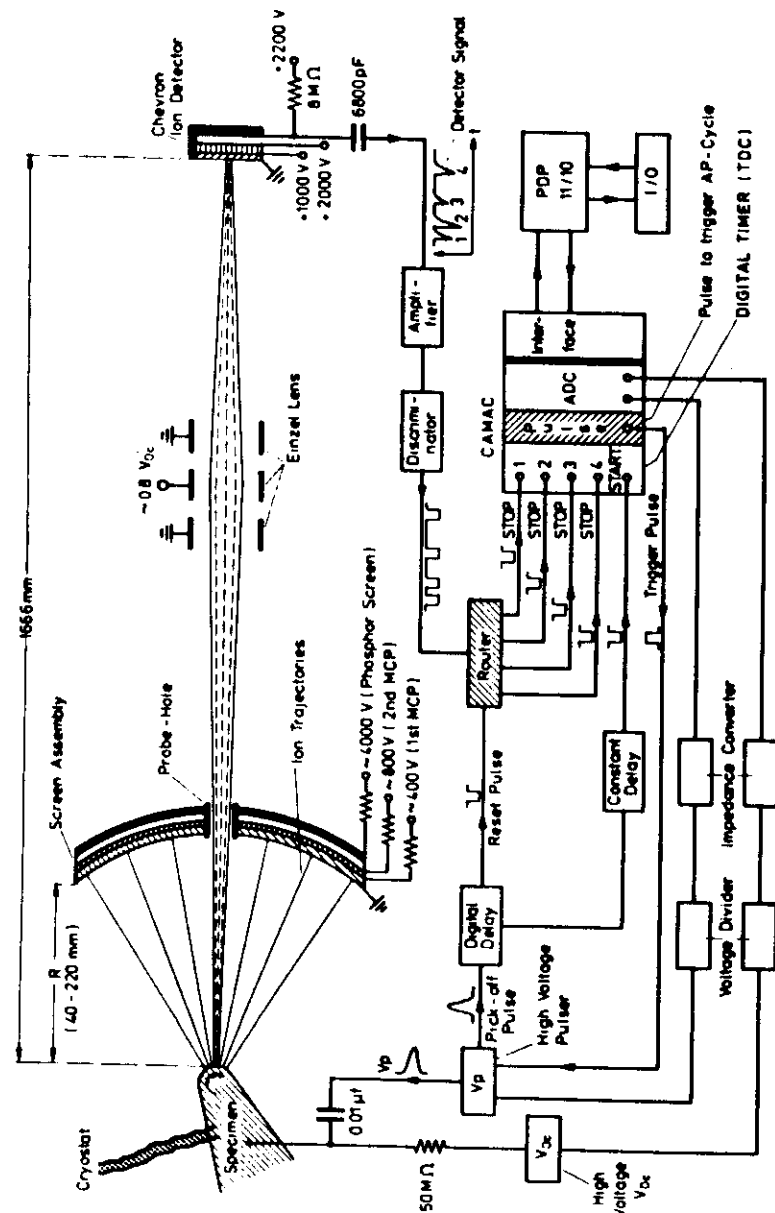


Figure 1 Atom-probe FIM operated at the University of Göttingen. The specimen is mounted on an x-y-z manipulator and attached to a cryostat filled with liquid N<sub>2</sub> via a flexible copper braid. The tip-to-screen distance ( $R$ ) can be varied between 40–200  $\mu$ m by shifting the FIM screen assembly (microchannel planes, MCP). The diameter of the probe-hole, which is internally grounded by a metal tube to avoid electrostatic deflections of the ion beam, is 2.5 mm. To maximize the ion yield per field-evaporated plane, the specimen is aligned with the instrument axis through x-y-z manipulation, until the current caused by randomly arriving imaging gas ions is at a maximum. The spread of the ion beam, which is imaged on the ion detector, is focused by adjusting the potential at the Einzel lens. Atom-probe control and data acquisition are performed by means of a computer that is interfaced to a CAMAC-system that consists of (a) a 4-channel 200-MHz clock (TDC) to measure the time-of-flight; the 4 channels of the clock are simultaneously started by a pulse which is synchronously picked off the high-voltage pulser. (b) A pulse module providing two pulses: (i) for triggering the high-voltage pulser, and thus, for initiating an atom-probe cycle, and (ii) to reset the router. If a sequence of ions (up to four), rather than a single ion, strikes the detector, the router assigns a stop signal from the first ion of the sequence to channel 1 of the TDC, the second one to channel 2, etc. (c) The ADC converter (ADC) measures  $V_p$  and  $V_{oc}$  during each atom-probe cycle.

The vacuum system basically consists of the specimen exchange chamber and the main chamber, which contains the FIM; they are separated by a straight-through valve. For easy and rapid specimen exchange without spoiling the vacuum in the main chamber, 11 specimens can be stored on a revolving plate in the specimen chamber. With respect to the vacuum system, the only provision made to incorporate the time-of-flight spectrometer into the FIM is a flight-tube with a detector housing at its end (7).

"effective probe-hole area"), enter the flight-tube of the atom-probe through the probe-hole. At the end of the flight-tube the ions reach the single-ion detector.

The typical FIM specimen is a sharply pointed needle with a radius of curvature ( $\bar{r}_t$ ) of about 20–80 nm. It is prepared from a thin wire of 0.1–0.3 mm diameter by anodic electropolishing (7). All heat treatments necessary for the particular phase transformation have to be performed prior to electropolishing.

After preparation, the specimen is introduced into the ultra-high ( $\sim 10^{-9}$  mbar) vacuum chamber of the FIM via a specimen airlock, mounted onto a manipulator, and cooled to  $\sim 80$  K in order to increase the resolution of the FIM image. The manipulator allows the specimen to be aligned along the axis of the instrument, and any region visible in the FIM image that is to be analyzed with the ToF spectrometer can be shifted until it covers the probe-hole of the atom-probe. The distance ( $R$ ) between tip vertex and the center of the screen can be varied typically between  $\sim 4$  and  $\sim 20$  cm allowing for a variation of the "average" magnification ( $\bar{M}$ ) in the FIM.  $\bar{M}$  is given by

$$\bar{M} = \frac{R}{\bar{r}_t} \times \beta'. \quad 1.$$

With typical values for the mean radius of curvature of the tip ( $\bar{r}_t$ )<sup>2</sup> and for  $R$  ( $\sim 3 \times 10^{-6}$  cm and  $\sim 4$  cm, respectively),  $\bar{M}$  is on the order of  $10^6$ .  $\beta'$  is approximately 0.6, which accounts for the fact that the FIM tip is not ideally hemispherical and, hence, the projection not purely gnomonic (18). Correspondingly, for the given values the effective diameter of the AP probe-hole ( $d_{ap}$ ) can be varied between  $\sim 3.2$  ( $R \sim 4$  cm) and  $\sim 0.8$  nm ( $R \sim 20$  cm).

To obtain FIM images of the alloys referred to in this article, neon, the imaging gas, is leaked into the vacuum system ( $\sim 5 \times 10^{-6}$  mbar). Subsequently, a positive high voltage ( $V_{DC}$ ), typically between 3 and 20 kV depending on  $r_t$ , is applied to the specimen. If the resulting electric field ( $F \approx V_{DC}/r_t$ ) exceeds a critical value ( $F_c \approx 30$  V/nm) the neon atoms are positively ionized in the high field regions above the tip surface, and are accelerated almost radially toward the grounded FIM screen, which lights up at the points of impact.

Starting with a freshly prepared tip, the electric field is highest above the sharp protrusions retained from the specimen preparation. As the voltage is gradually increased, the electric field above these protrusions reaches a value  $F_{FE} > F_c$  at which local "field evaporation" (18) of individual atoms in the

<sup>2</sup> Both  $\bar{r}_t$  and the local radius of curvature can be determined quite accurately directly from FIM micrographs (7).

form of  $n$ -fold charged ions occurs ( $n = 1$  or 2 for most transition metals) (7). Since the onset of field evaporation occurs at a certain field strength, regions with smaller radii of curvature field evaporate earlier than those with larger ones. Thus, field evaporation is used to smooth a freshly prepared FIM specimen until the atomically smooth, curved tip-end required for ultimate resolution in the FIM images is finally obtained.

## 1.2 Image Formation and Contrast of Decomposed Alloys

The mechanism of image formation is illustrated in Figure 2. In the high-field regions of the FIM tip, the neon atoms become polarized and are therefore attracted to the positively charged tip surface. After several inelastic collisions with the cool surface, the polarized, hopping gas atoms are finally ionized by the tunneling of an electron from the gas atom through a potential barrier, and into the specimen. The tunnel probability is highest at a distance  $x_0$ , approximately 0.5 nm above the tip surface, where the energy of the electron lies at, or slightly above, the Fermi energy of the metal. The smallest electric field sufficient to ionize the neon atoms is reached only above atoms protruding from the surface. In pure metals these protruding atoms are usually located in ledge, or kink-site positions (Figure 2) at the edges of different stacks of lattice planes. The edges of one stack of  $hkl$  planes form almost concentric polygons, or rings, because of the intersection of each stack with the more or less spherically shaped tip surface (Figure 2). This arrangement of atoms with localized high-field regions lead to the well-known crystallographic pattern of FIM micrographs of pure metals and dilute alloys (Figure 3a).

In most two-phase alloys the precipitates appear in either bright or dark

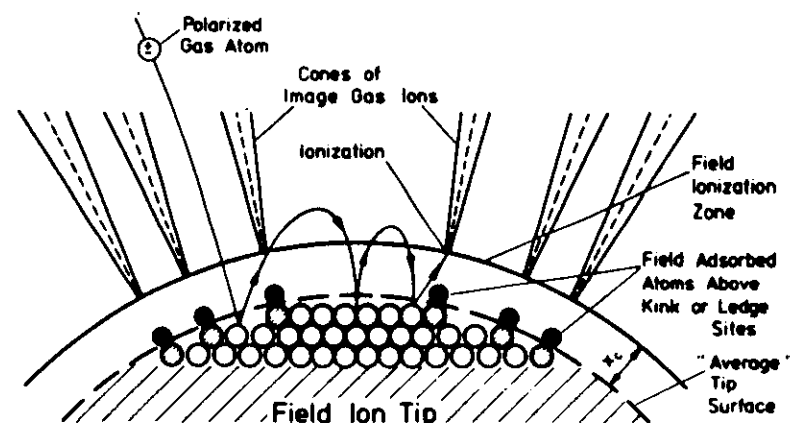


Figure 2 The principle of field-ion image formation: only the hatched atoms are imaged.

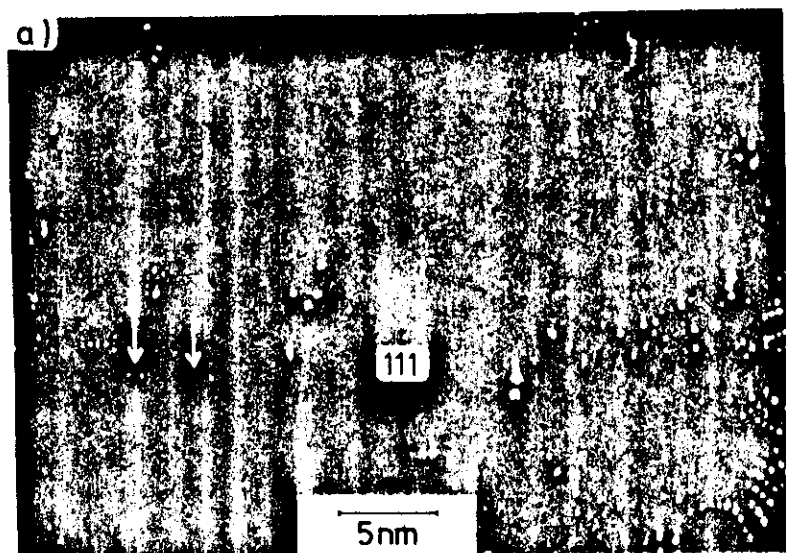


Figure 3 Neon field-ion image of Cu-1 at.% Fe aged for 100 min at 500°C. Arrows indicate nuclei of a metastable iron-rich precipitate phase (a). The same alloy after aging for 150 min (b). Note the enhanced contrast of the Fe-rich clusters and the reduced resolution of the matrix as compared to (a) (25).

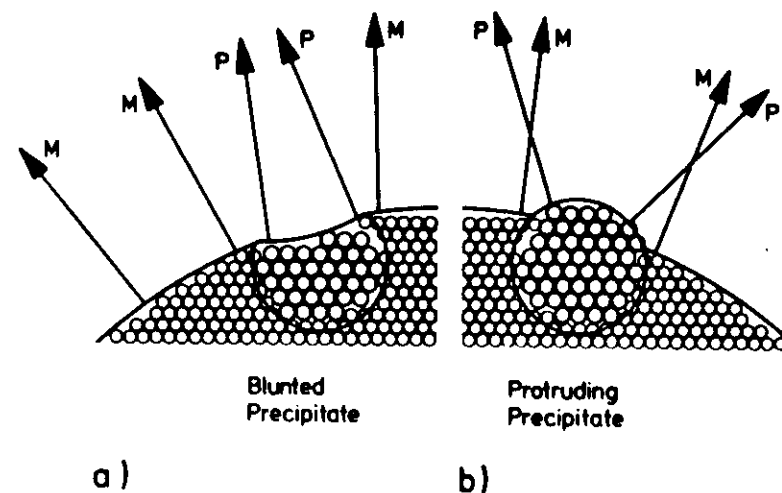


Figure 4 Surface topology around precipitates after the tip reaches a steady-state end-form. (a) blunted precipitates appear in dark contrast; (b) protruding precipitates appear in bright contrast. Also, the trajectories of field-evaporating ions, originating from the matrix (M) or the precipitate (P), are shown schematically.

contrast to the surrounding matrix. In both cases, after some field evaporation a steady state end-form of the FIM tip evolves, with the precipitates either protruding from the emitter surface (i) or being blunted (ii) as compared to the local radius of curvature of the adjacent matrix (Figure 4). These local deviations in the radius of curvature above the precipitates are caused by a respectively higher (i) or lower (ii) evaporation field than is necessary to field evaporate the surrounding matrix. Although not yet fully understood, it is assumed that the electric field variations associated with variations in surface topology, caused by the precipitate, are responsible for an enhanced (i) or reduced (ii) ionization probability above the precipitates and, hence, a bright or dark contrast, respectively. Copper-rich precipitates in Fe-Cu show a dark contrast; gold-rich precipitates, which are more resistant to field evaporation than the surrounding matrix, appear bright in Fe-Au imaged with neon (19). However, the contrast of a particular phase can also depend on the image gas and the temperature of the tip. For instance, the Cu-rich particles in an Fe-Cu alloy become bright if imaged with hydrogen instead of neon. Gamma-prime precipitates of the type  $(\text{Ni-Co})_3(\text{Al-Ti-Cr})$  in a Ni-based superalloy exhibit bright contrast at a tip temperature of 80 K (Figure 5), whereas hardly any contrast is seen at 30 K (20). On the other hand, no contrast is obtained from  $\gamma'\text{Ni}_3\text{Al}$  particles in a binary Ni-14 at.% Al alloy

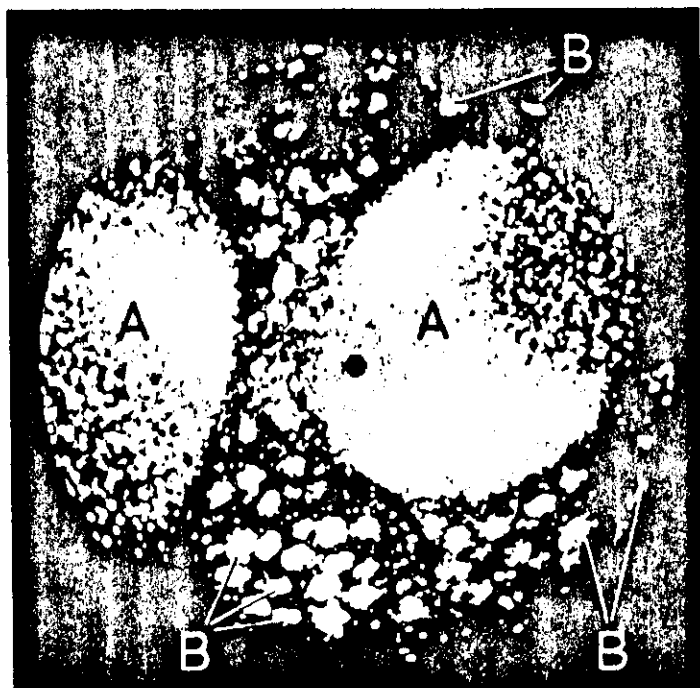


Figure 5 Neon field-ion image of a nickel-based superalloy after a four stage heat treatment. It exhibits two large (A) and many small (B)  $\gamma'$  precipitates (6). (Courtesy P. A. Beaven.)

(21). Apparently, the processes of field ionization and evaporation are highly sensitive to the composition of the precipitates.

FIM images of certain other alloys, e.g. Cu-5 at.% Ti or Co-Ta, aged in the two-phase region of the phase diagram, look similar to those of one-phase materials, and do not reveal any precipitate contrast, despite the evidence of AP analyses and TEM, which have clearly established the presence of second-phase particles. Figure 6a shows a rather regular field-ion image of a Cu-5 at.% Ti specimen aged for 6 h at 350°C; no discrete particles are seen. However, after a rupture in part of the tip, suddenly the precipitated phase (dark contrast in Figure 6b) can be clearly distinguished from the bright matrix. Following some field evaporation the contrast between the two phases disappears again. These peculiar contrast features are not observed in less concentrated, aged Cu-1.9 at.% Ti where the  $\text{Cu}_4\text{Ti}$  particles always appear in dark contrast, Figure 6c (22). Similar changes in the appearance of the phase contrasts have been reported for Co-Ta (23). In aged Co-7.5 at.% Ti no obvious signs of precipitation are visible with fairly

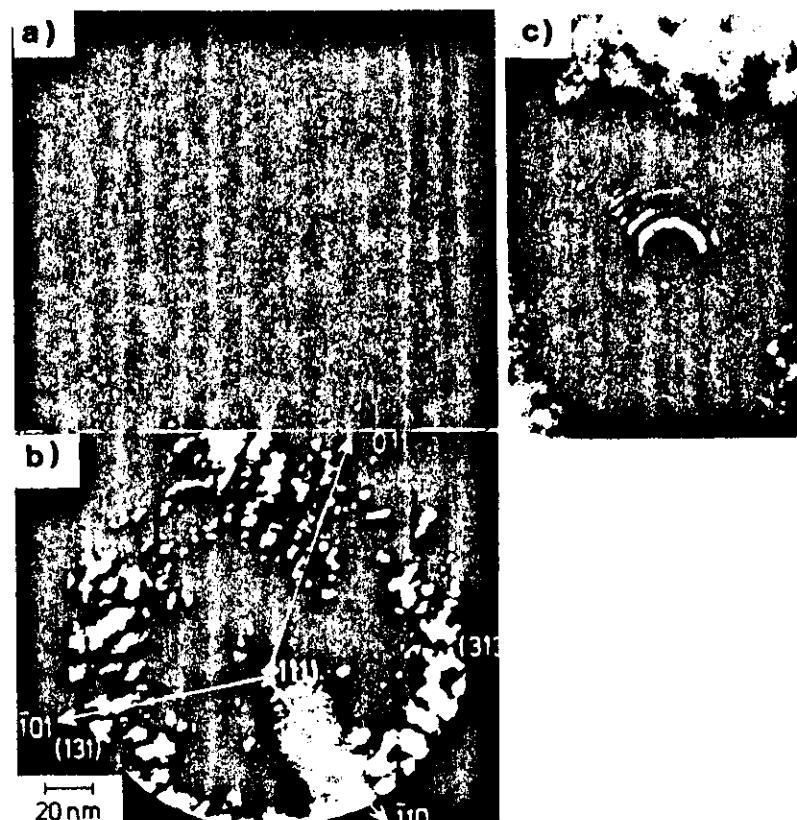


Figure 6 Neon field-ion images of Cu-5 at.% Ti aged for 6 h at 350°C before (a) and after (b) part of the tip has ruptured. Only in b do the two phases appear in contrast. Figure 6c shows Cu-1.9 at.% Ti aged for 5 min at 350°C.  $\text{Cu}_4\text{Ti}$  are discernible by their dark contrast (22). (For better reproduction of c, the contrast of some Ti-enriched clusters was artificially enhanced.)

sharp tips ( $r_t \lesssim 40$  nm) (24). However, after blunting the tips to about 80 nm by continuous field evaporation, the  $\text{Co}_3\text{Ti}$  precipitates become visible.

These examples demonstrate that the absence of any precipitation contrast in the FIM pattern does not necessarily mean that the alloy has not yet decomposed into two distinct phases. In alloys where the precipitated phase is not visible, one must rely on atom-probe analysis (following section) to investigate the state of phase separation.

The contrast features of field-ion images of decomposing alloys also frequently depend on the degree of decomposition. This is shown in Figures 3a and 3b for a Cu-1 at.% Fe alloy (25). After aging the alloy for 100 min at

500°C, the matrix is still atomically resolved, and the contrast of the precipitates is rather faint (a). After aging for 150 min, the atomic resolution of the matrix atoms (Cu) is lost, but the contrast of the precipitates is strongly enhanced (b). The contrast enhancement in later stages of the precipitation reaction, at the expense of image resolution of the matrix, has been observed quite frequently in various two-phase alloys.

Because of the localized change in the radius of curvature above precipitates (Figure 4), a considerable unknown change in the magnification ( $M$ ) of the particular precipitate results (Equation 1). If the precipitates are nonspherical, e.g. thin platelets or  $\gamma'$  zones, the magnification can even be rather anisotropic. Therefore, it is generally not possible to determine the size of (visible) particles directly from an FIM micrograph just by using the average magnification ( $\bar{M}$ , Equation 1).

Nevertheless, the size and morphology of visible precipitates can often be determined very accurately without knowing  $M$  by using the *persistence-size* technique (Figure 7a). By controlled field evaporation several lattice planes of a previously identified pole ( $hkl$ ) are successively removed. Whenever a precipitate becomes visible in the vicinity of this pole, the number of planes ( $n_{hkl}$ ) that have to be evaporated between the appearance and disappearance of the particle are counted. The dimension of the precipitate along the ( $hkl$ ) direction is then immediately obtained as  $d(hkl) \times n_{hkl}$ , with a depth resolution of  $\sim 0.2$  nm. By recording the variations in intersectional area of the precipitate with the tip surface during the dissection of the precipitate, its morphology can be determined in detail.

### 1.3 Atom-Probe Analyses

The chemical identification of a single ion is achieved by first measuring its time of flight ( $t$ ), and subsequently evaluating its mass-to-charge ratio ( $m/n$ ) (Figure 1). For this purpose the atoms are field evaporated at a well-defined instant by superposing a high-voltage pulse of a few nanoseconds rise-time onto the tip, which is held at the imaging voltage ( $V_{DC}$ ) (pulse field evaporation). A pulse width of about 15 nsec and a pulse amplitude ( $V_p$ ) of about  $0.15 V_{DC}$  are found to be appropriate for the analysis of most alloys. Due to the sharp drop in field strength within a few nm above the tip surface, the field-evaporated ions reach their terminal velocity ( $v$ ) shortly after the desorption event. The ions then drift with an energy

$$n \times e(V_{DC} + V_p) = \frac{1}{2}mv^2 = \frac{1}{2}m \frac{d^2}{t^2}, \quad 2.$$

over a distance ( $d$ ) virtually equal to the tip-to-detector distance (Figure 1). After a time-of-flight  $t$ , they strike the ion-detector. In essence, Equation 2

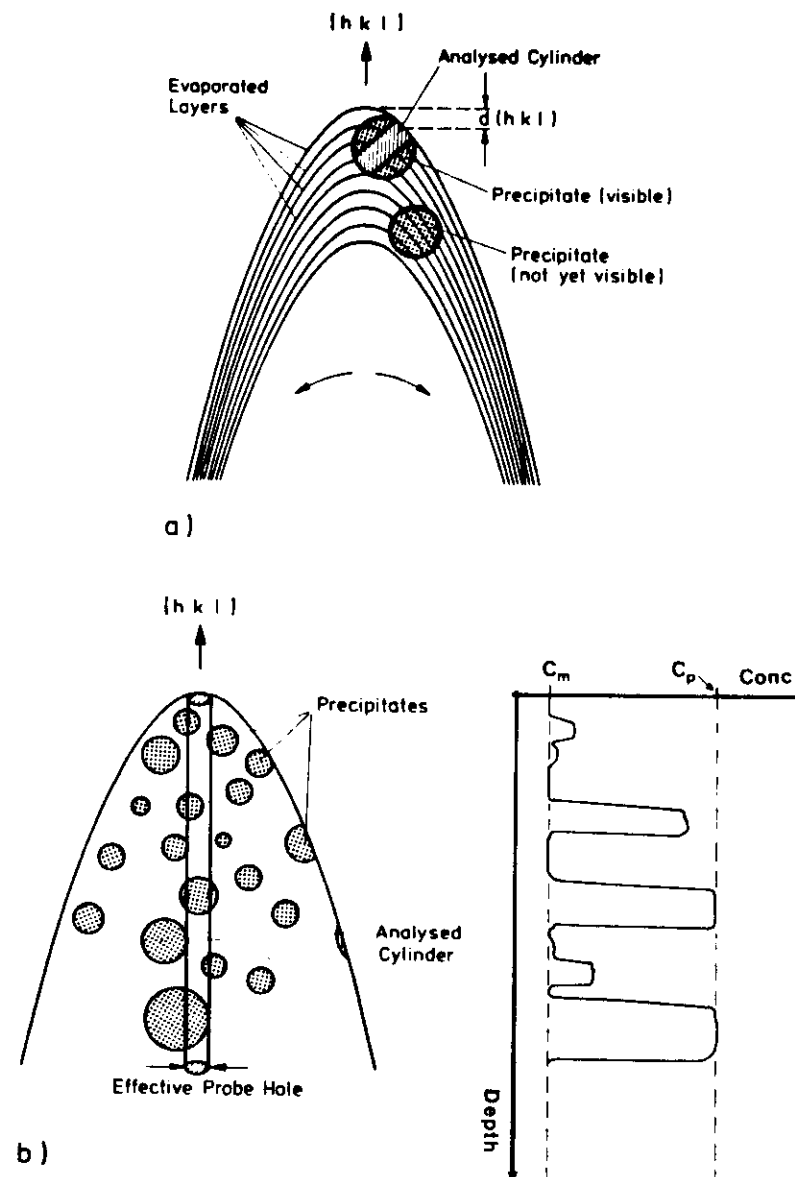


Figure 7 (a) "Persistence-size" technique for the accurate determination of the size and morphology of visible precipitates. The principle of selected area AP analysis of a visible precipitate is also illustrated. In (b), the nearly cylindrical volume analyzed during a "random-area" AP analysis, and the resulting composition profile are shown. Only some particles are completely cut by the cylinder.

already contains all measurable quantities for the evaluation of  $m/n$ ; however, in practice, electronic delay times, pulse shape factors, etc (7) have to be taken into account in order to operate the AP at its optimum mass resolution. For most instruments the latter is of the order  $\Delta m/m \approx 1/150$ , but can be improved significantly (to about 1/1000) by employing an *energy focusing* ToF spectrometer (26) rather than a conventional one.

In principle, the quantitative microanalysis of decomposing alloys using the atom-probe can be performed in two different ways. The first of these is *selected area analysis* (Figure 7a). This type of analysis of the composition of individual particles is confined to precipitates that are discernible in the FIM image. By rotation of the FIM specimen, the particular precipitate is imaged over the probe-hole in the FIM screen. If the effective probe-hole (diameter  $d_{ap}$ ) is larger than the particle,  $d_{ap}$  is decreased by increasing the magnification until the precipitate covers the probe-hole entirely. The composition of the precipitate is then determined by collecting the atoms originating from a cylinder of diameter  $d_{ap}$ , and of a length limited by the total depth that can be probed before the precipitate has been completely field evaporated (Figure 7a). By continuing to probe into the adjacent matrix to determine the composition of each successively removed lattice plane, the concentration profile across interphase boundaries can also be obtained. As discussed in the previous section, with this method the size and detailed morphology can be determined rather precisely. The accuracy of this compositional analysis depends on the total number of atoms that can be collected from the precipitate. For small particle sizes, such as occur in early precipitation stages, several particles have to be analyzed in order to keep the confidence limits narrow. This requires a sufficient number density of particles, e.g.  $\geq 10^{17} \text{ cm}^{-3}$ .

The second technique is *random-area analysis* (Figure 7b). In order to analyze the composition and distribution of particles that are not visible in the FIM, or to obtain information about solute fluctuations in alloys (e.g. spinodally decomposing alloys), it is necessary to determine the concentration profile in a cylinder of considerable length. The cylinder should be more than 100 nm long in one direction ( $h'k'l'$ ), with a sufficient depth resolution (Figure 7b). For this purpose, the planar concentration of each successively field-evaporated  $h'k'l'$ -lattice plane is determined and plotted against the number of evaporated planes. Hence, the depth resolution is equal to the interplanar spacing  $d(h'k'l')$ . Whenever the analyzed cylinder cuts completely through a particle (Figure 7b), its composition and the solute variation across its interphase boundary can be determined directly from the concentration profile. However, if the particle is partly cut by the analyzed cylinder (Figure 7b), the concentration profile reveals only a local increase in the solute content as compared to the surrounding matrix ( $c_m$ ).

but does not give any information about the true composition of the particle ( $c_p$ ).

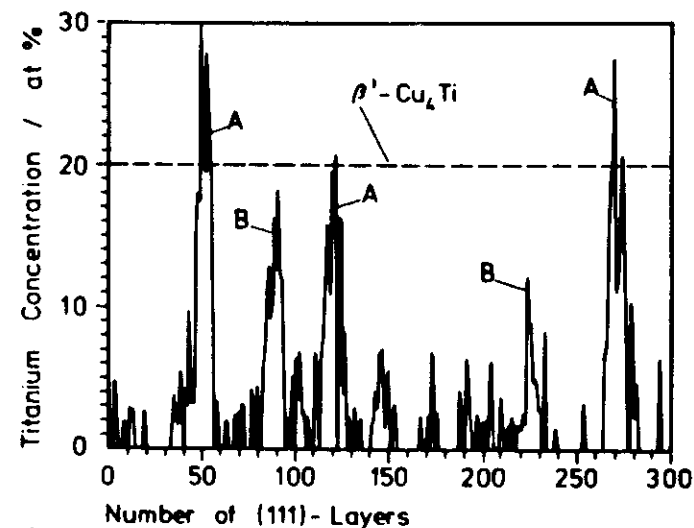
Figure 8a shows the composition profile along [111] of an aged Cu-2.7 at.% Ti alloy that contains isolated  $\beta'$   $\text{Cu}_4\text{Ti}$  precipitates. Three particles (A) are completely cut, and two are probably only partly cut (B) by the analyzed cylinder ( $d_{ap} \approx 2.5 \text{ nm}$ ). The considerable statistical noise superposed on the actual composition profile results chiefly from the limited number ( $N$ ) of atoms that can be collected per field-evaporated plane. For  $d_{ap} \approx 2.5 \text{ nm}$ ,  $N$  typically fluctuates between 50 and 120. If ultimate depth resolution of one interplanar spacing is not required, e.g. for slowly varying composition profiles, smoothing of the measured composition profiles can be achieved by summing up the atoms from several successively field-evaporated planes. Small solute clusters that were not unambiguously discernible in the original, blurred AP composition profile can often be deconvoluted through a moving-average analysis; this is another smoothing technique (7). These smoothing procedures, in fact, remove the high frequency components of the original AP composition profile, but also flatten the concentration profiles across interphase boundaries. Therefore, prior to applying any smoothing procedures, the original composition profile, recorded with ultimate depth resolution but rather poor statistics, must be carefully inspected.

By analogy with the analysis-of-time series, the data contained in an AP composition profile are often analyzed in terms of an autocorrelation analysis, provided the distance probed through the specimen is sufficiently large. This statistical analysis furnishes most decomposition parameters that are required for a comparison with theoretical predictions (see following section). During the early stages of phase separation when cluster sizes are small and their number densities large this method is especially useful. Figure 8b shows the autocorrelation coefficient  $R(k)$  for the concentration profile displayed in Figure 8a.  $R(k)$  is given by

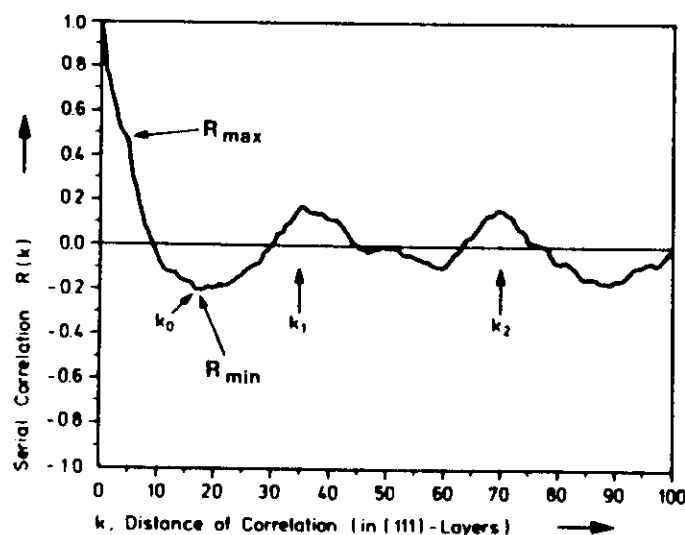
$$R(k) = \frac{n}{n-k} \frac{\sum_{i=1}^{n-k} (c_i - c_0)(c_{i+k} - c_0)}{\sum_{i=1}^n (c_i - c_0)^2}, \quad 3.$$

where  $c_i$  is the concentration of the  $i$ -th field-evaporated plane ( $h'k'l'$ ),  $c_0$  the mean concentration,  $n$  the total number of field-evaporated planes, and  $k$  is the correlation length in units of the interplanar distance  $d(h'k'l')$ . From computer-simulated atom-probe analyses for which various precipitate microstructures were assumed, it has been established that the parameters  $k_0$ ,  $k_1$ ,  $R_{\max}$ , and  $R_{\min}$  (Figure 8b) are unequivocally related to the mean





a)



b)

Figure 8 (a) Concentration profile along  $[111]$  of a Cu-2.7 at.% Ti specimen aged for 500 min at 350 °C. On the average, 50 atoms per field-evaporated (111) plane were collected. One removed (111)-layer corresponds to a probing depth of 0.18 nm. Particles completely or only partly cut by the analyzed cylinder are denoted by A and B, respectively. (b) Corresponding correlogram (28).

particle diameter ( $2 \times \bar{R}$ ), the interparticle distance ( $\lambda$ ), the particle composition ( $c_p$ ), and the precipitate volume fraction ( $f$ ), respectively (27). In particular, computer-simulations yielded  $\lambda = k_1 \times d(h'k'l')$ , and  $2\bar{R} = k_0 \times d(h'k'l')$  for larger particles (e.g.  $\bar{R} \gtrsim 1.2$  nm). For size distributions with even smaller mean radii, autocorrelation analyses yield  $\bar{R}$  values somewhat larger than the true ones. In Figure 8b, the occurrence of the second peak at  $k_2$  is at exactly twice the distance of the first peak, indicating that  $\text{Cu}_4\text{Ti}$  particles are quasiperiodically distributed (28). For randomly distributed, solute-rich clusters of small number density  $R(k)$  remains zero for  $k > k_0$ .

The true composition of a solute-rich cluster is only displayed in a composition profile if the cluster is *completely* covered by the probe-hole (see Figure 7b); this requires  $d_{ap} < 2\bar{R}$ . Although in principle  $d_{ap}$  can be made as small as one atomic diameter, reliable statistics require that a certain number of atoms be recorded, hence  $d_{ap}$  is on the order of  $\sim 2$  nm. Therefore, in most real analyses of composition fluctuations, the lateral spatial resolution is confined to  $\sim 2$  nm (7).

It is worth noting that both  $\bar{R}$  and  $\lambda$  can be obtained from autocorrelation analyses regardless of whether the ratio  $d_{ap}/2\bar{R}$  is larger or smaller than unity. Also, the Fourier transform of the autocorrelation factor  $R(k)$  yields the (one-dimensional) structure factor  $S(q)$  obtained from scattering experiments ( $q$  is a wave vector). Thus, in principle, a random-area AP analysis furnishes all the information about the state of decomposition that can be inferred from  $S(q, t)$ , as determined in a SAXS or SANS scattering experiment.

## 2. RESULTS ON VARIOUS ALLOYS

### 2.1 Modes of Decomposition

As indicated in the previous section, the AP is particularly suited to the study of the decomposition of alloys on a very fine scale. In order to slow down the kinetics to an observable rate, these materials are usually quenched deep into the two-phase field, and the correspondingly large supersaturations then create second-phase nuclei typically 2 nm in diameter. As applied so far, this is below the resolution of conventional transmission electron microscopy. Neutron and X-ray small angle scattering (SAS) are, on the other hand, well suited to the observation of such small particles. For a comparison of the three methods, as applied to the decomposition of alloys, see the proceedings of a recent topical conference (29). The problem with SAS is that it does not reveal the composition of the particles formed, but only their sizes and number density. This is a distinctive feature that differentiates the two modes of *homogeneous*

decomposition (the only type of decomposition reviewed here). The two modes of homogeneous decomposition are detailed below.

In the *nucleation and growth* mode (NG), small particles that differ greatly from the composition of the matrix form by thermal fluctuations, and then grow in size. They are surrounded by a depletion zone in whose concentration gradient the solute diffuses "downhill" to the particle and makes it grow. The other mode, *spinodal decomposition* (SD), involves long-range composition modulations, often periodic ones, that enlarge in amplitude with time, and also somewhat in wavelength, until the final second-phase composition, as prescribed by the phase diagram, or a metastable phase is reached. The solute diffuses "uphill" in the concentration gradient in this case.

The second-phase particle distribution will be the same in the later stages according to both decomposition modes: A distribution of final-composition particles that is often periodic. In NG the solute depletion around particles enforces, along with other factors, finite particle spacings. Thus, a typical scattering experiment does not indicate whether the mechanism of particle formation was NG or SD. It is the initial particle composition, and only this feature (7), that differentiates the two.

It is well known that in the central part of a two-phase field the thermodynamic factor and, accordingly, the chemical diffusion coefficient become negative, which encourages SD. In the peripheral region, close to the solvus, NG decomposition is necessary. The two regions are separated by the spinodal curve, whose definition and practical existence has been doubted in recent times (12). The theoretical spinodal position also depends on the strain energy accompanying the decomposition; it moves to low  $T$  at large misfit strains. The kinetics of both decomposition modes have been studied by AP. The theories explaining these kinetics are summarized next.

## 2.2 Theories of NG Kinetics

According to the classic Becker-Vollmer theory (30), the formation of a coherent second-phase ( $\beta$ ) nucleus in a homogeneous matrix ( $\alpha$ ), involving no size misfit, necessitates the formation of an interface of specific energy  $\sigma_{\alpha\beta} > 0$ , as well as a gain in chemical free energy ( $\Delta f_v$ ) per unit volume of  $\beta$ . For a sphere of radius  $R$ , those two terms depend on different powers of  $R$ , therefore a barrier must be overcome, which defines a critical nucleus of size

$$R^* = \frac{2\sigma_{\alpha\beta}}{\Delta f_v}, \quad \text{and of extra free energy} \quad \Delta F^* = \frac{16\pi\sigma_{\alpha\beta}^3}{3\Delta f_v^2}. \quad 4.$$

This energy is supplied by thermal fluctuations with a stationary rate per

unit volume of

$$I_\infty = DN \frac{N_2}{N_3} \left( \frac{\Delta F^*}{3\pi kT} \right)^{1/2} \exp \left( - \frac{\Delta F^*}{kT} \right). \quad 5.$$

Here  $D$  is the solute diffusion coefficient in the matrix,  $N$  the atom number density, and  $N_2$  and  $N_3$  are the atomic numbers in the surface and volume of the critical nucleus, respectively. This nucleation rate builds exponentially to the value  $I_\infty$ , with a time constant  $\tau$  at least equal to the time needed for the B atoms to diffuse together, i.e.  $\tau \geq R^{*2} \times 2/D$ .

Once the nucleus is over the critical size it grows from its own matrix environment with a rate given by  $R \approx \sqrt{Dt}$  (31). This rate holds for a short period, until the depletion spheres of neighboring particles overlap. Then competitive "Umlösung" (Ostwald ripening) starts, as described in its asymptotic limit ( $t \rightarrow \infty$ ), by the classical Lifshitz-Slyozow-Wagner (LSW) theory (32, 33). Accordingly, the mean radius of the size distribution grows as

$$\frac{dR^3}{dt} = b = \text{const}, \quad 6.$$

while the supersaturation  $\Delta C$  (assumed to already be small) decreases as

$$\Delta C = (\kappa t)^{-1/3}. \quad 7.$$

In principle, from the constants  $b$  and  $\kappa$  the two parameters of the coarsening kinetics,  $D$  and  $\sigma$ , can be evaluated. However, in the range of validity of the LSW theory ( $\Delta C \rightarrow 0$ ),  $\Delta C$  is too small to be measured reliably with the AP or any other technique. Hence, frequently only the product  $D\sigma$  can be determined from  $b$ .

In practice, the nucleation period is not clearly separated from the coarsening period, so that attempts have been made to describe both processes in a unified theory (8, 9). The number density ( $N_v$ ) of particles generally changes with time by nucleation, and simultaneously by dissolution due to a changing critical radius. Thus,

$$\frac{dN_v}{dt} = I(t) - N(R = R^*, t) \frac{dR^*}{dt}, \quad 8.$$

where  $N(R, t)$  is the size distribution of the particles. The mean particle radius,

$$\bar{R} = \frac{1}{N_v} \int_{R^*}^{\infty} N(R) R \, dR,$$

changes as

$$\frac{d\bar{R}}{dt} = v(R) + \frac{1}{N_v} I[R^*(t)] (R^* - \bar{R}) + (\bar{R} - R^*) \frac{N(R^*)}{N_v} \frac{dR^*}{dt},$$

with

$$v(R) = \frac{D}{\bar{R}} \frac{\bar{c}(t) - C_R}{C_\beta - C_R} \quad 9.$$

accounting for diffusive growth or dissolution.

The solute concentrations in the matrix and the particle are  $c$  and  $C_\beta$ , respectively.  $C_R$  is the concentration directly over a particle of radius  $R$ , according to Gibbs-Thomson

$$C_R = C_\infty \exp\left(\frac{2\Omega\sigma}{RkT}\right), \quad 10.$$

where  $\Omega$  is atomic volume, and  $C_\infty$  represents the equilibrium solubility.

Together with the continuity equation, the equations of motion for  $N_v$  and  $\bar{R}$  (Equations 8 and 9) have been solved numerically (8, 9) under certain assumptions, in particular those concerning the long-term coarsening behavior, the particle size distribution, and the constancy of  $D$  and  $\sigma$ .

A priori, it is not possible to assess the influence of these assumptions on the precipitation kinetics results. Therefore, an algorithm (or "numerical model") has recently been devised (9) that describes the entire course of precipitation within the framework of existing nucleation and growth theories. No simplifying assumptions enter this algorithm; in particular it allows the time evolution of  $N(R, t)$  to also be computed. A comparison with experimental results is given later.

### 2.3 Theories of SD Kinetics

Cahn's theory of SD kinetics (10) is conceptually much simpler than that of NG, as it basically involves only diffusion, though uphill, and contains no further stochastic element. [Subsequently, Cook (34) has added a thermal fluctuation term to the theory.] Cahn starts with Fick's law (in one dimension)

$$\frac{\partial c}{\partial t} = \tilde{D} \frac{\partial^2 c}{\partial x^2} = D \left[ \frac{c(1-c)}{kT} \frac{\partial^2 F}{\partial c^2} \right] \frac{\partial^2 c}{\partial x^2}. \quad 11.$$

Here in the thermodynamic factor [...] for  $F$ , the so-called gradient-energy density  $k(dc/dx)^2$  has to be included to account for the high price of very short wave concentration modulations. This leads, in the linearized form of Cahn's theory (considering the coefficients in Equation 11 to be constant),

to a term  $\partial^4 c / \partial x^4$  in Equation 11. Beginning the solution with a Fourier ansatz, certain components will grow exponentially and determine the positions of the evolving precipitates in three dimensions. This growth law is rarely observed; instead, a much slower power law growth, and a slow increase of the dominant wavelengths with time are seen. This fits the pattern predicted by later nonlinear, though numerical, theories (11, 12). Another matter of debate is the behavior of the system as it approaches the spinodal ( $\partial^2 F / \partial c^2 = 0$ ) from either side (29).

### 2.4 AP Studies of Decomposition by NG

After the pioneering papers of Goodman et al (35) on FeCu, quite a number of quantitative studies have been made available.

**2.4.1 Ni-Al** An alloy of Ni-14 at.% Al decomposes at 823 K, and forms  $\gamma'$   $\text{Ni}_3\text{Al}$  precipitates coherently with the fcc  $\gamma$  matrix (21). The particles are not directly visible in the FIM (Section 1), but are only discernible in the recorded AP composition profiles (e.g. Figure 8). These particles have been analyzed by the statistical method of autocorrelation, together with computer simulation (Section 1), to yield  $\bar{R}$  and the precipitated volume fraction  $f$  or  $N_v$ . As there are relatively few particles in the analyzed volume, it is difficult to get the particle size spectrum  $N(R)$  directly. The solute concentration ( $C_\beta$ ) of particles having diameters smaller than the probe-hole size (i.e.  $2\bar{R} \leq 2.5$  nm) could not be determined directly from the composition profiles, but also had to be inferred from joint autocorrelation and computer simulation analyses.

One of the most important results is that even the smallest observed precipitates, of radius 10 Å or smaller, have the equilibrium composition Ni-23 at.% Al. This suggests an NG, not an SD character, as has previously been claimed (36). It is interesting to note that at the shortest observed aging times the activation barrier ( $\Delta F^* \approx 4kT$ ) is relatively small. The thermochemistry of the system is sufficiently known to evaluate  $\Delta f_v$  as a function of supersaturation. Also,  $\sigma$  has been measured from overaging kinetics of larger particles, thus  $R^*$  can be calculated as a function of the directly measured  $\Delta C(t)$ , and compared with the AP results on  $\bar{R}(t)$ . The data obtained at 550°C are shown in Figure 9; they prove that nuclei have been observed. This appears to be the first such observation for a solid-solid diffusive phase transformation.

Figure 10 shows the aging time evolution of the particle density, compared with the one expected from time integration of the nucleation rate. It is evident that there is no pure nucleation stage, but that Ostwald ripening intervenes after a short aging time. Therefore, the unified theories discussed in Section 2.2 are needed to interpret the experimental data.

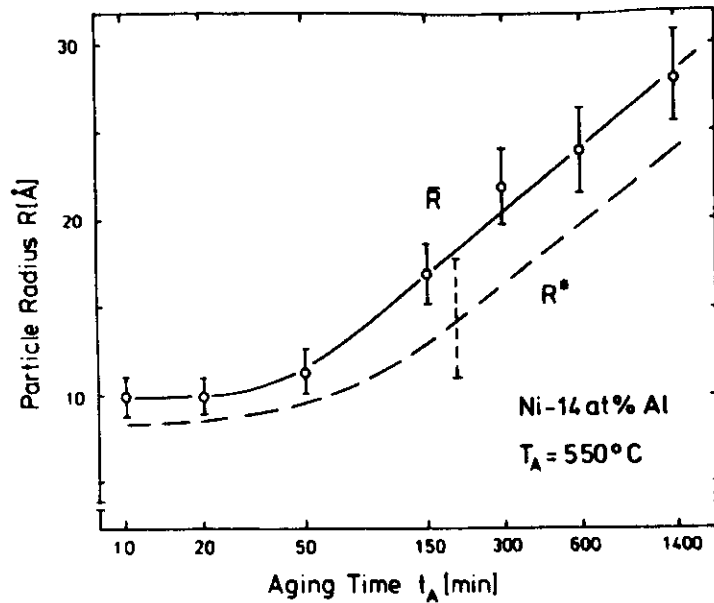


Figure 9 Measured mean particle radius and calculated radius of critical nuclei versus aging time (21).

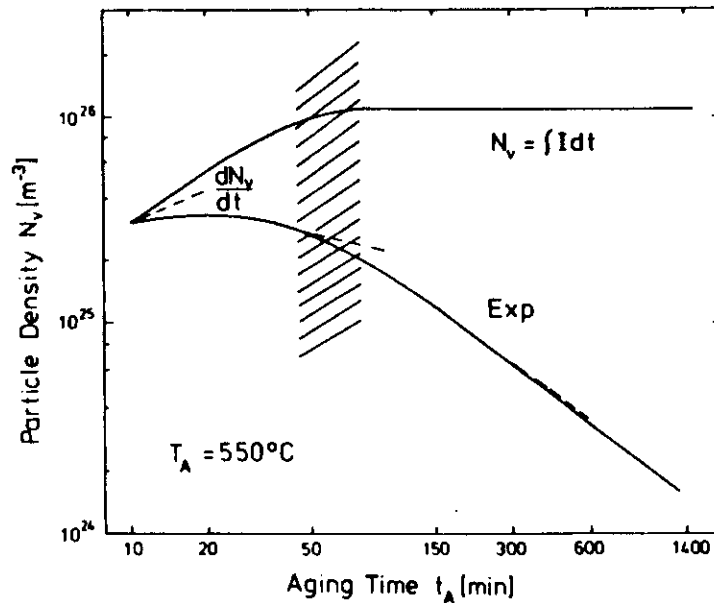


Figure 10 Experimental number density of particles in Ni-14 at.% Al, and calculated density of nucleated particles versus aging time (21).

Figure 11 shows  $\bar{R}(t)$  and  $R^*(t)$  calculated according to the Langer-Schwartz theory (8), modified to apply far from the critical point (9). The modified theory (MLS theory) uses the nonlinear version of the Gibbs-Thomson equation, and accounts for an incubation time in the nucleation rate (9). Also shown are the results from the "numerical model" (9), which allows the kinetics to be computed more accurately from the precise knowledge of  $N(R, t)$ , at each stage of the phase transformation. By fitting the theoretical curves to the experimental data, both  $\sigma$  and  $D$  can be determined rather accurately. Interestingly, the initial plateau in  $\bar{R}(t)$  shows up more strongly in the experiments than in the "numerical model." This probably indicates a limit on the minimum observable particle size in the statistical analysis of AP concentration profiles.

Experimental and theoretical results for the time ( $\tau_h$ ) needed to complete half of the decomposition reaction, i.e. reduce  $\Delta C$  to half its initial value, are shown in Figure 12. At the high (relative) supersaturation ( $y_0$ ) used here,  $\tau_h$  is the time needed to overcome resolution effects caused by overaging rather than by nucleation itself, which dominates at small  $y_0$ . In addition, an evaluation of the incubation time of nucleation (9) indicates that clusters of Al atoms diffuse together and disperse again several ( $c_w$ ) times before a critical nucleus is formed.

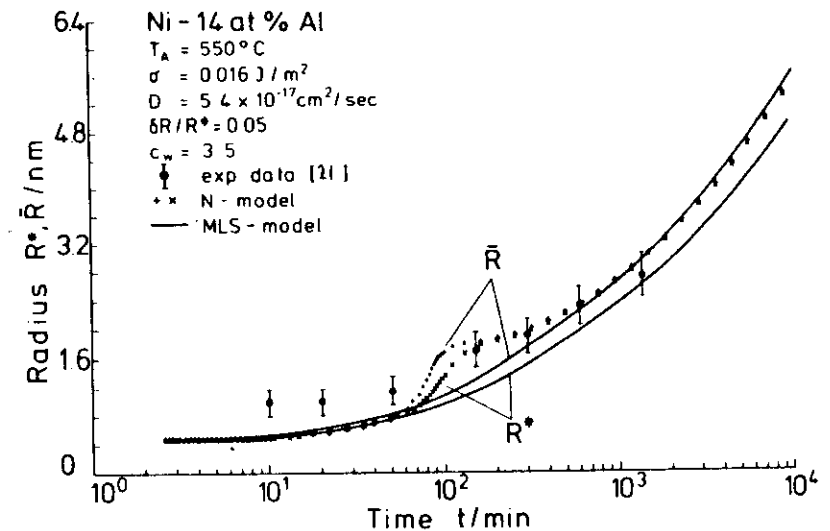


Figure 11 Fit of numerical model (9) and modified Langer-Schwartz model (8) to mean particle radius  $\bar{R}$  versus aging time in Ni-14 at.% Al (21).  $R^*$  = calculated radius of nuclei. For other parameters see text.

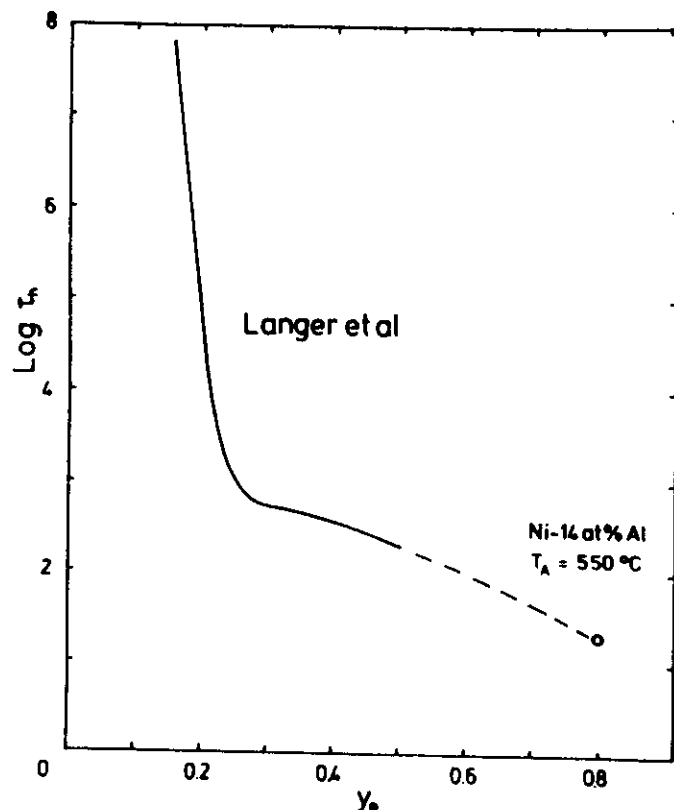


Figure 12 Half-time of decomposition versus normalized supersaturation according to theory (8) and experiment (21).

2.4.2 Ni-Cu-Al The Ni 36% Cu 9% Al alloy (37) is interesting because in the ternary various nonconodal paths of decomposition are possible in principle, and the third component may enrich the particle interface. Again, there is very little misfit between the  $\gamma'$  precipitate and the fcc  $\alpha$  matrix. In this alloy FIM does image the two phases in different contrast (Section 1, Figure 13), so particle diameters can be measured more directly, and compared with those analyzed from concentration profiles. Particles of the equilibrium composition  $(\text{Ni}_8\text{Cu}_2)_3\text{Al}$ , at 580°C, are found at the very earliest aging times.

Of particular interest is the composition profile across a particle interface, as measured by AP (Figure 14). The composition changes very sharply at the interface (within three lattice planes); this is expected thermodynamically for the relatively low aging temperature. Becker's



Figure 13 FIM image of decomposed Ni 36 at.% Cu 9 at.% Al after aging for 420 min at 580°C (37).

nearest-neighbor interaction model leads one to expect  $\sigma = 18 \text{ mJ m}^{-2}$  for Ni-Ni<sub>3</sub>Al; the measured value is  $16 \text{ mJ m}^{-2}$ . For the ternary alloy  $\sigma = 52 \text{ mJ m}^{-2}$  is found. The large change upon adding Cu remains mysterious. There is some enrichment of Cu in the (NiCu)/(NiCu)<sub>3</sub>Al interface (Figure 15), but this seems to be a nonequilibrium kinetic feature, as Al diffuses faster than Ni and Cu, but the sum of Ni and Cu concentrations remain constant.

Again, the kinetics of nucleation and growth have been studied in detail and compared with the unified theories. In the case of Ni-Cu-Al, some

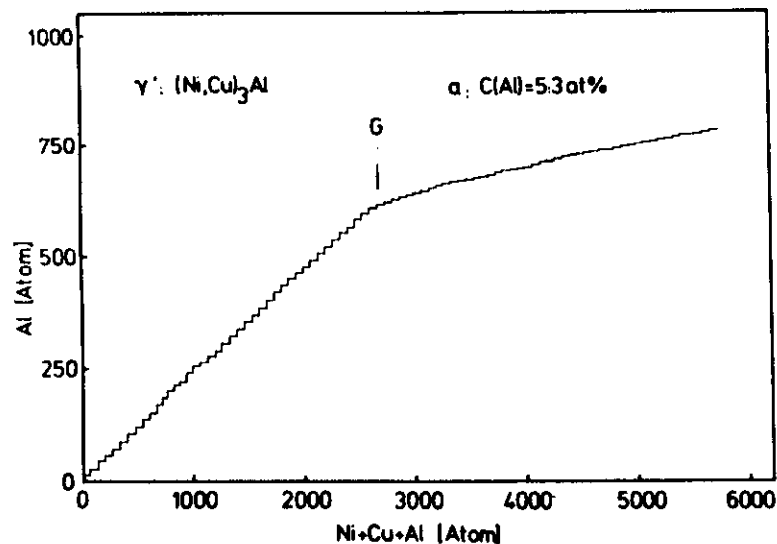


Figure 14 Interface composition profile of precipitate in Ni 36%Cu 9%Al measured as number of field-desorbed Al atoms per total number of atoms (37) in 420 min at 580°C.

particle size distributions have been measured; they are found to be 2–3 times wider than that calculated by LSW (32, 33). In this alloy the work of nucleation,  $\Delta F^*/kT = 27$  at 540°C, or 16 at 500°C, is much larger than in Ni–Al. Diffusion coefficients determined from the aging kinetics are on the order  $10^{-16} \text{ cm}^2 \text{ s}^{-1}$ , and are not influenced by quenched-in vacancies, which should be annealed out long before the aging times considered here.

One last point of interest is the observed distribution of particle distances. It is a Poisson-type distribution, with a standard deviation of about 60% that of a random distribution; thus showing a tendency toward a regular spacing, as discussed above.

**2.4.3 Cu–Fe** The hardening of Cu by 1.15% Fe was studied (25) as a function of precipitated volume fraction and particle radius, using FIM measurements. Again, the particles are visible with FIM because of their contrast with the matrix. During aging at 500°C, the particle radius remains constant ( $\bar{R} = 0.6 \text{ nm}$ ) for the first 150 min while the particle density grows. This behavior appears to be typical for many NG decomposing alloys studied with FIM.

**2.4.4 Cu–1.9 at.% Ti** Aging of Cu–Ti alloys of Ti contents between 0.5–5 at.%, at  $T = 300\text{--}450^\circ\text{C}$  leads to the formation of metastable, ordered,  $\text{Cu}_4\text{Ti}$  precipitates (22, 38). The FIM images of Cu–1.9 at.% Ti aged for only

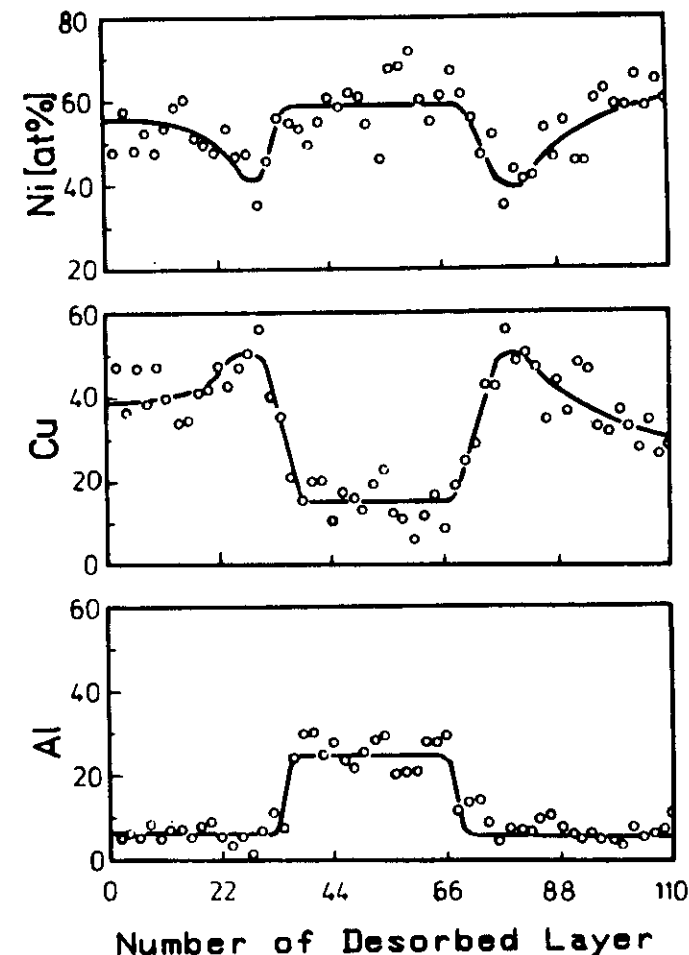


Figure 15 Composition profiles across precipitate in Ni 36 at.% Cu 9 at.% Al.

2.5 min at 350°C reveal many discrete precipitates ( $\bar{R} \approx 1 \text{ nm}$ ), with sharp interphase boundaries in black contrast (e.g. Figure 6). An extensive FIM and AP analysis of the precipitation kinetics led to the conclusion that at 350°C, Cu–1.9 at.% Ti decomposes via an NG reaction. As shown in Figure 16, the “numerical model” describes the experimental data rather well for  $\sigma = 67 \text{ mJ m}^{-2}$ , and  $D = 2.5 \times 10^{-15} \text{ cm}^2 \text{ s}^{-1}$  (9, 22). The large value of  $\sigma$ , relative to the one in Ni–Ni<sub>3</sub>Al, and the correspondingly large  $\Delta F^* \approx 7kT$  makes for a relatively short nucleation period. Neither the nucleation period ( $t < 1 \text{ min}$ ), nor the stage at which coarsening follows the

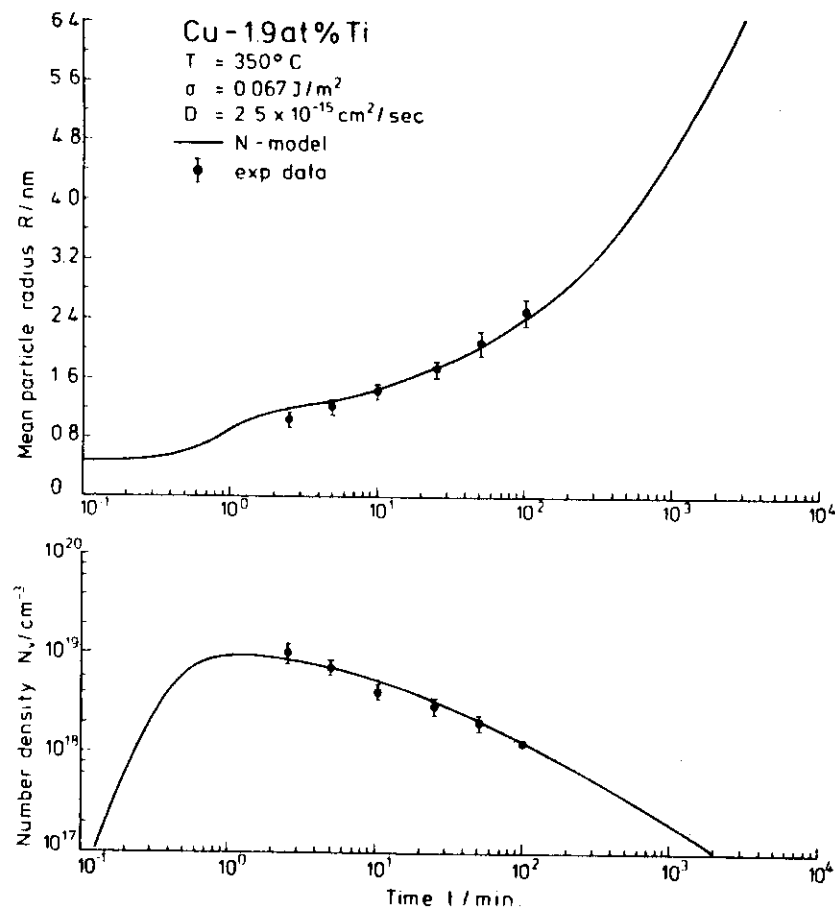


Figure 16 Fit of numerical model to particle radius and particle density versus aging time in Cu-1.9 at.% Ti (22).

LSW kinetics ( $t > 10^5$  min), are covered by the experimental period ( $2.5 \leq t \leq 10^2$  min) (9).

Because of the relatively large  $\Delta F^*$  in Cu-1.9 at.% Ti, the nuclei rapidly attain sizes outside the range in which particle growth is dominated by stochastic processes, i.e.  $d\bar{R}/dt \gg dR^*/dt$ . Theoretically, this situation—relative to that of Ni-Al, where  $\bar{R}$  cannot escape from  $R^*$ —is advantageous for the unified theories (Section 2.2). These theories face difficulties when nucleation, which they describe as a stochastic process, and growth or redissolution, described in a deterministic way, intervene significantly (9).

It is worth noting that the value for  $D$  is larger, by a factor of about 350, than the interdiffusion coefficient obtained by extrapolating the available high temperature data to  $350^\circ\text{C}$ . This strongly positive deviation of  $D$  at low temperatures from an Arrhenius plot is not presently understood. However, it appears to be typical of alloys undergoing phase separation at low homologous temperatures (22).

## 2.5 AP Studies of SD

**2.5.1 Cu-Ti** Aging of Cu-Ti alloys of Ti contents between 0.5 and 5 at.%, at  $T = 300$ – $450^\circ\text{C}$ , leads to the formation of ordered  $\text{Cu}_4\text{Ti}$  precipitates. Based on the modulated precipitate microstructure observed in the TEM, it was concluded that decomposition of the more concentrated alloys is continuous, i.e. of the SD type. As stated above, this criterion is not sufficient to exclude a NG mechanism, so AP was used (22, 28, 38) to establish the evolution of Ti concentration amplitude and wavelengths in a number of alloys. Recently, SANS was also applied to these alloys.

Decomposition of Cu-2.7 at.% Ti at  $350^\circ\text{C}$  has been studied with the AP FIM (28). Since the second-phase particles were not clearly discernible in the FIM, extended AP composition profiles were recorded and analyzed by statistical models. Aging for 10 min at  $350^\circ\text{C}$  led to the formation of small Ti-rich clusters with mean diameters of  $2\bar{R} \approx 1.1$  nm, and a mean center-to-center spacing (or mean composition modulation wavelength) of  $\lambda \approx 2.8$  nm.  $\bar{R}$  and  $\lambda$  grew from the beginning according to  $\bar{R} \approx t^{1/4}$ , and  $\lambda \approx t^{1/3}$  (Figure 17a, b). For  $t < 50$  min, the diameter of the clusters remained smaller than that of the probe-hole used for the AP analyses ( $d_{ph} \approx 2.5$  nm). Therefore, the true Ti amplitude of the composition modulations could not be determined directly from the AP composition profiles, but rather had to be inferred from a comparison of the measured profiles with those obtained from computer simulations (22, 28). Using this procedure, the maximum Ti concentration of the clusters appeared to increase continuously (Figure 17c) until it reached 20 at.%, as expected for  $\text{Cu}_4\text{Ti}$  after  $t \approx 50$  min. (At this stage  $d_{ph}/2\bar{R} \approx 1$ , thus, the Ti concentration could be determined directly from the composition profiles.) The apparently continuous increase of the Ti concentration of the incipient precipitates can be taken as evidence for an SD reaction. It must be emphasized, however, that the results displayed in Figure 17c were derived under the assumption that for  $t < 50$  min the composition waves have a sinusoidal form. According to the figure, after 10 min of aging the Ti-enriched clusters ( $2\bar{R} \approx 1.1$  nm) contain only about four Ti atoms. This number appears to be too small to be reliably deconvoluted from the composition profiles, which are blurred by statistical noise. Hence, the results shown in Figure 17c for  $t \leq 25$  min should be regarded with caution.

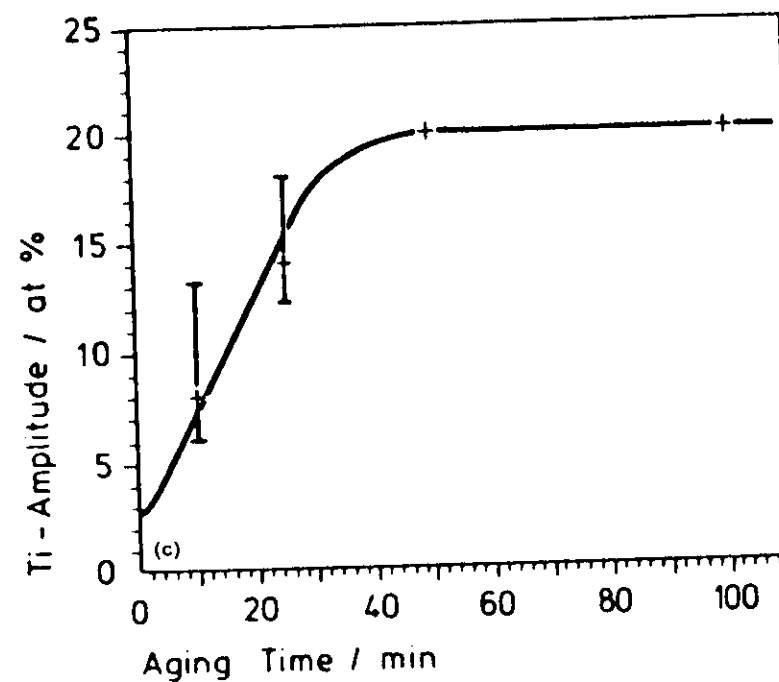
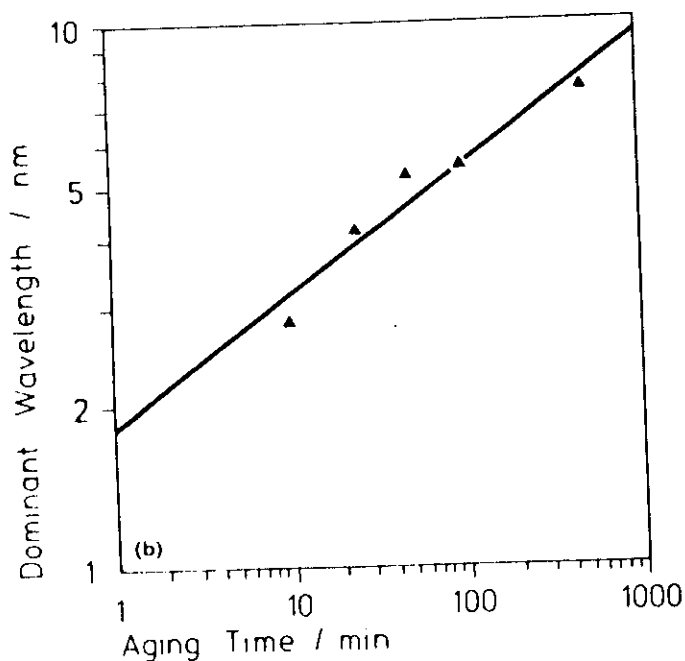
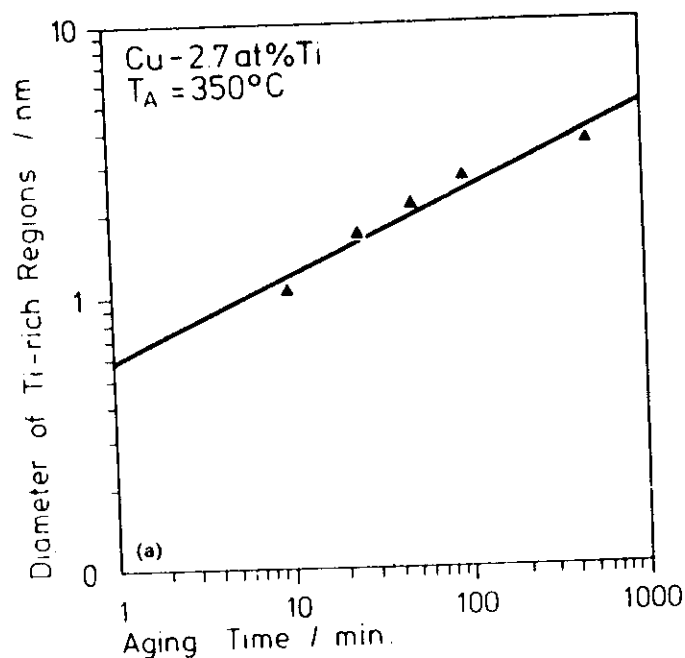


Figure 17 Measured parameters characterizing spinodal microstructure versus aging time at  $350^\circ\text{C}$  in Cu-2.7 at.% Ti (28).

**2.5.2 Fe-Be** In this system a low temperature miscibility gap involves the formation of an ordered Fe-Be phase (B2) from a bcc iron-rich solid solution. The Fe-25 at.% Be alloy studied in the FIM (39) was aged at  $350^\circ\text{C}$ . It shows a beautiful macrolattice of brightly imaged, isolated, cubical, iron-rich particles, aligned along  $\langle 100 \rangle$ , in agreement with TEM observations (Figure 18). The microstructure coarsens according to a time law  $d^n - d_0^n = kt$ ,  $n = 2, \dots, 3$ . The  $\sigma$  composition is likely to be of the SD type, although the regular array of iron-rich particles could also be the result of the considerable misfit strain involved ( $\sim 4\%$ ).

**2.5.3 Fe-Cr-Co** Alloys of Fe 28% Cr 15% Co, with minor additions of 1% Al, and 0.25% Zr, are useful as ductile permanent magnets (CHROMINDUR). They derive from the Fe-Cr phase diagram, which decomposes into two bcc phases (called  $\alpha_1$  and  $\alpha_2$ ) if the  $\sigma$  phase is suppressed (especially by the Co addition). The Co also extends the miscibility gap to a higher temperature, and makes it asymmetric toward the Fe side. The aging cycle used in optimum permanent magnet



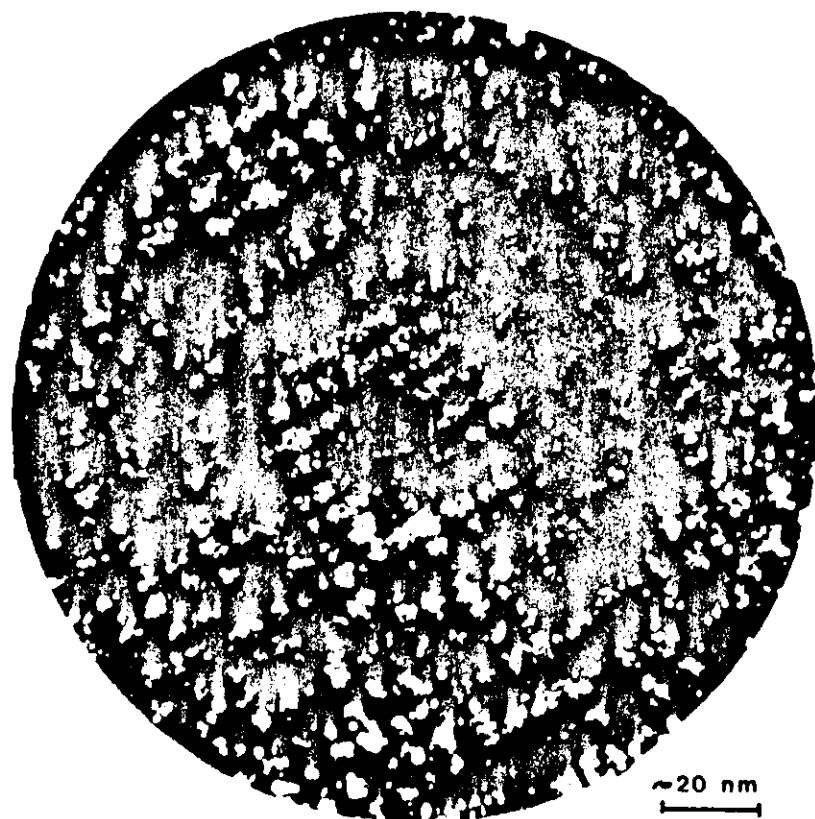


Figure 18 Neon FIM image of Fe 25% Be aged for 2 h at 350°C. (Courtesy S. S. Brenner, Pittsburgh.) (39).

production [to give the maximum energy product  $(BH)_{\max}$ ] is rather complicated. It involves aging in a magnetic field just below the Curie temperature, and critical temperature of the gap, i.e. at 625°C, and further aging at 525°C, to increase the concentration amplitudes. The resulting microstructure of the optimum magnet is shown in Figure 19 (40, 41). The Fe-rich phase images brightly, the Cr-rich phase darkly.

As one field evaporates the tip of the sample in the AP, one follows the contiguity of the two phases in depth. Both phases are sponge-like, interconnected, and do not resemble iron-rich ellipsoids in a chromium-rich matrix, as assumed in the elongated single-domain (ESD) theory of permanent magnets. In the ESD theory, the magnetization of a ferro-

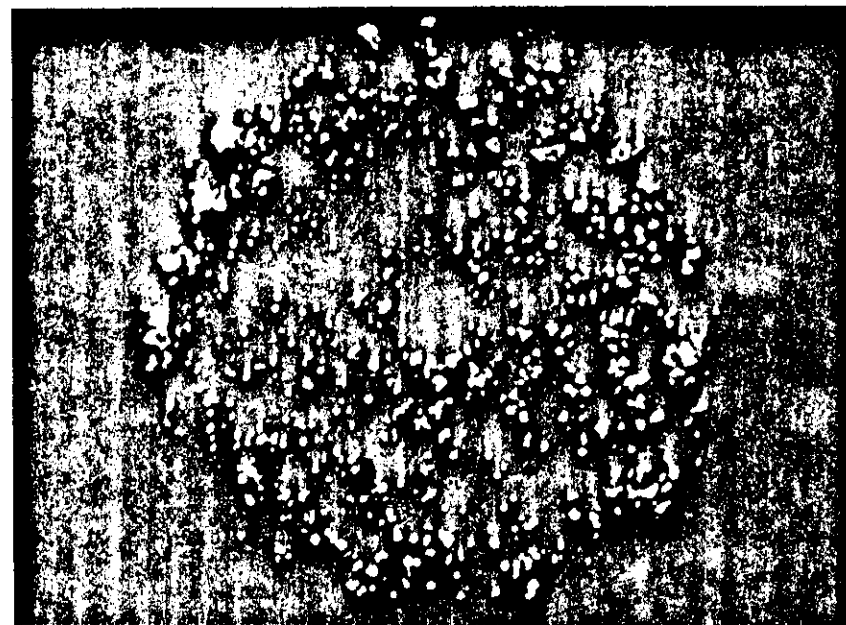


Figure 19 Neon FIM image of CHROMINDUR after aging to optimum magnetic hardness (40).

magnetic phase is fixed to the long axis of the ellipsoid, which is isolated from its neighbors by a paramagnetic matrix. This model also does not apply because *both* phases are ferromagnetic, according to inferences from AP analyses. Figure 20 gives in-depth concentration profiles for Fe, Cr, and Co; the Al seems to follow the Fe, as does the cobalt. It is clear that where Cr enriches, Fe and Co move out. The composition of  $\alpha_1$  is Fe 6% Cr 22% Co, and that of  $\alpha_2$  is Cr 26% Fe 6% Co. The latter composition is, in fact, weakly ferromagnetic at 300 K, with an estimated Curie temperature of 80°C. The volume of  $\alpha_2$  is 40%.

The kinetics of decomposition is followed separately during aging at 600°C or 525°C. As seen in Figure 21, the Cr concentration amplitude in the dark phase changes slowly with time, as expected for SD. The periodicity ( $\lambda$ ) and mean thickness of  $\alpha_2$  regions also increase slowly with time, according to a  $t^{0.24}$  law. Again, this agrees with nonlinear SD theory. The coercivity of such a microstructure must derive from Bloch wall pinning, the walls find lower energy positions in the dark than in the bright phase. The decomposition of Fe-Cr itself was also studied recently (42). "Alnico" magnets were also investigated by AP FIM (43).

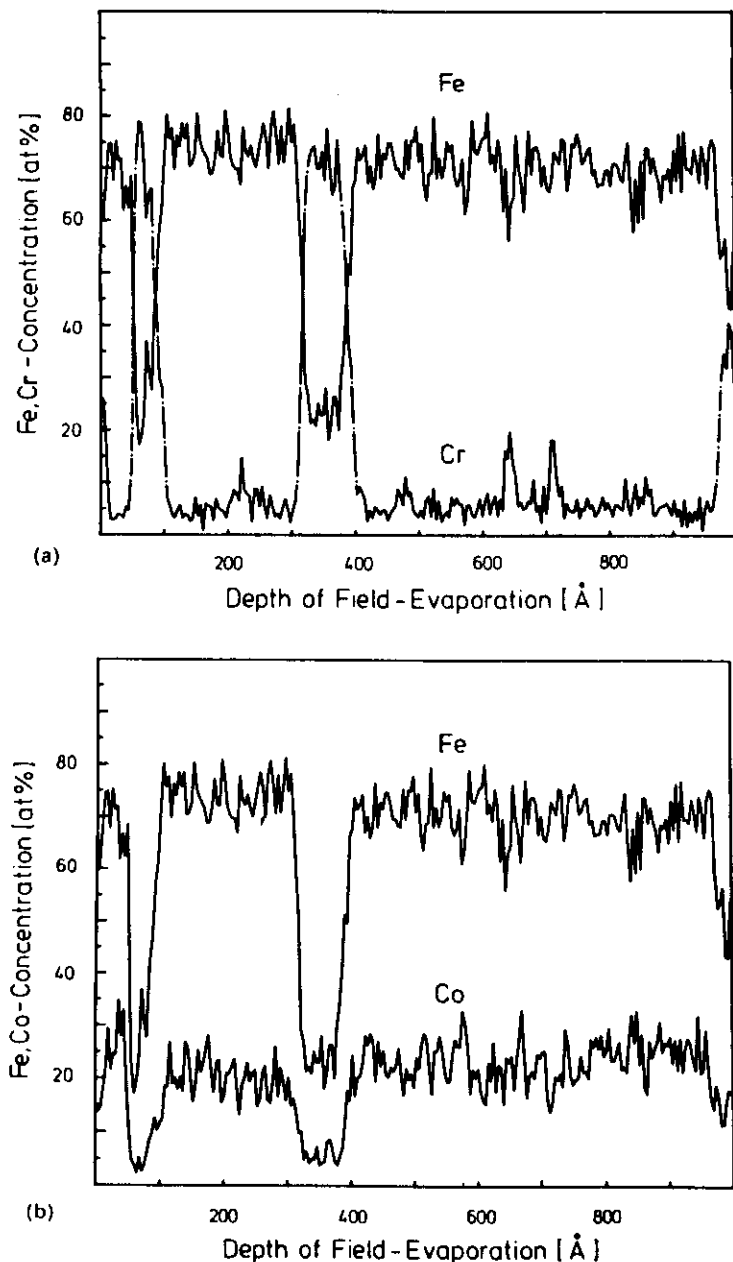


Figure 20 Concentration profiles of CHROMINDUR after aging to optimum magnetic hardness (40). Abscissa is depth of evaporation in nm.

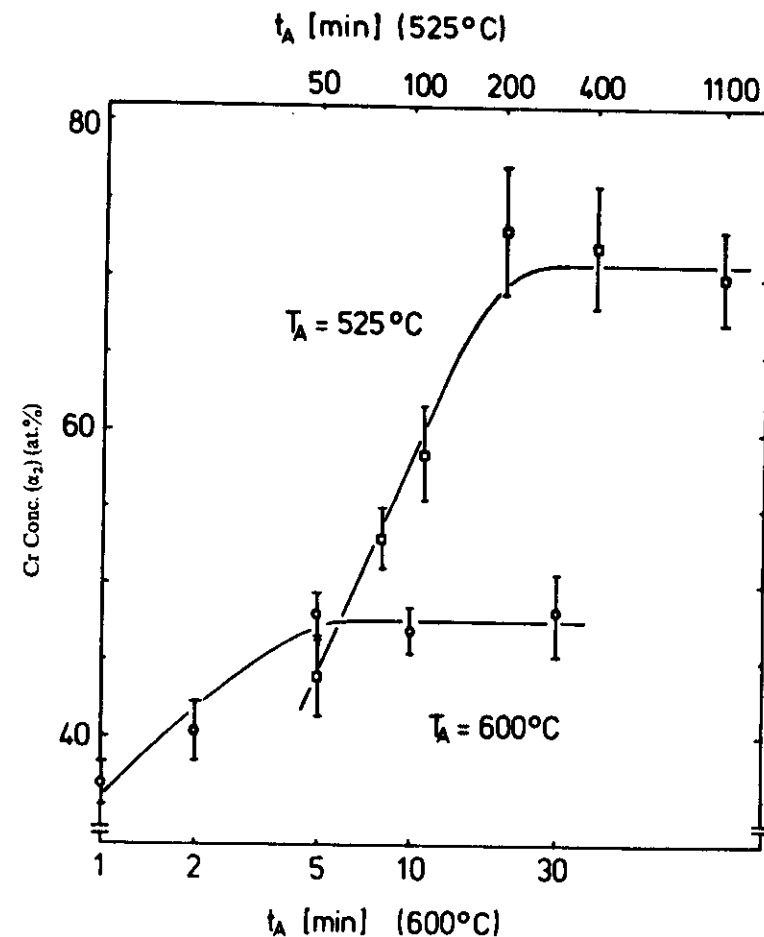


Figure 21 Chromium concentration in dark ( $\alpha_2$ ) phase of Fe 28 at.% Cr 15 at.% Co 1 at.% Al versus aging time at two temperatures (40).

## 2.6 Conclusions

The above examples of alloy systems whose decomposition has been studied by AP FIM clearly show the extensive interaction between theory and experiment made possible by the new technique. In the case of NG, considerable understanding and agreement have been reached; however, this is still lacking for the spinodal type of decomposition. Here both theoretical and experimental efforts are badly needed.

## ACKNOWLEDGMENT

P. Haasen is grateful to Stanford for its hospitality during the tenure of the Walter Schottky Professorship. Both authors acknowledge the contributions of their colleagues R. Kampmann, H. Wendt, J. Piller, L. von Alvensleben.

## Literature Cited

- Müller, E. W., Panitz, J. A., McLane, S. B. 1968. *Rev. Sci. Instrum.* 39: 83
- Miller, M. K., Smith, G. D. W. 1977. *Met. Sci. J.* 11: 249
- Turner, P. J., Papazian, J. M. 1973. *Met. Sci. J.* 7: 81
- Andrén, H.-O., Henjered, A., Nordén, H. 1980. *J. Mater. Sci.* 15: 2365
- Wagner, R., Brenner, S. S. 1978. *Acta Metall.* 26: 197
- Beaven, P. A., Miller, M. K., Smith, G. D. W. 1977. *Proc. Inst. Phys. Conf. Ser.* 36: 199. London: Inst. Physics
- Wagner, R. 1982. *Field-Ion Microscopy in Materials Science. In Crystals: Growth, Properties and Applications*, Vol. 6, pp. 1-116. Berlin: Springer-Verlag
- Langer, J. S., Schwartz, A. J. 1980. *Phys. Rev. A* 21: 948
- Kampmann, R., Wagner, R. 1984. See Ref. 29, p. 91
- Cahn, J. W. 1968. *Trans. AIME* 242: 166; 1966. *Acta Metall.* 14: 1685
- Langer, J. S., Baron, M., Miller, H. D. 1975. *Phys. Rev. A* 11: 1417
- Binder, K., Billotet, C., Mirol, P. 1978. *Z. Phys.* 30: 183
- Wagner, R. 1981. *Czech. J. Phys. B* 21: 198
- Brenner, S. S., McKinney, J. T. 1970. *Surf. Sci.* 23: 88
- Andrén, H.-O., Nordén, H. 1979. *Scand. J. Metall.* 8: 147
- Hall, T. M., Wagner, A., Seidman, D. N. 1977. *J. Phys. E* 10: 884
- Miller, M. K., Beaven, P. A., Smith, G. D. W. 1979. *Surf. Interface Anal.* 1: 149
- Müller, E. W., Tsong, T. T. 1969. *Field Ion Microscopy*. New York: Elsevier
- Brenner, S. S., Miller, M. K. 1980. *Proc. Int. Field Emiss. Symp.*, ed. Y. Yashiro, N. Igata. Tokyo: Univ. Tokyo. 238 pp.
- Beaven, P. A., Delargy, K. M., Miller, M. K., Smith, G. D. W. 1978. *Proc. Int. Congr. Electron Microscopy, Toronto*, 1: 626. Ontario: Microscop. Soc. Canada
- Wendt, H., Haasen, P. 1983. *Acta Metall.* 31: 1649
- von Alvensleben, L., Wagner, R. 1984. See Ref. 29, p. 143
- Youle, A., Ralph, B. 1972. *J. Microsc.* 95: 309
- Davies, D. M., Ralph, B. 1972. *J. Microsc.* 96: 343
- Wendt, H., Wagner, R. 1982. *Acta Metall.* 30: 1561
- Müller, E. W., Krishnaswamy, S. V. 1974. *Rev. Sci. Instrum.* 46: 1053
- Piller, J., Wendt, H. 1982. *Proc. 29th Int. Field Emiss. Symp.*, ed. H.-O. Andrén, H. Nordén, p. 265. Stockholm: Almqvist & Wiksell
- Biehl, K.-E., Wagner, R. 1981. *Proc. Int. Conf. Solid-Solid Phase Transf.*, ed. H. I. Aaronson, D. E. Laughlin, R. F. Sekerka, C. M. Wayman. Warrendale, Penn: Met. Soc. AIME, p. 185
- Haasen, P., Gerold, V., Wagner, R., Ashby, M. F., eds. 1984. *Decomposition of Alloys: The Early Stages, Acta Metall. Ser. Metall. Conf. Series*. Oxford: Pergamon. Vol. 2, pp. 1-239
- Russell, K. C. 1970. In *Phase Transformations*, 6: 219. Metals Park, OH: ASM
- Ham, F. S. 1958. *J. Phys. Chem. Solids* 6: 335
- Wagner, C. 1961. *Z. Elektrochem.* 65: 581
- Lifshitz, T. M., Slyozov, V. S. 1961. *Phys. Chem. Solids* 19: 35
- Cook, H. E. 1970. *Acta Metall.* 18: 297
- Goodman, R. S., Brenner, S. S., Low, J. R. 1973. *Metall. Trans. A* 4: 2363, 2371
- Hill, S. A., Ralph, R. 1982. *Acta Metall.* 30: 2219
- Liu, Z. G. 1984. *Nachr. Gött. Akad. Wiss.* 2: 13; Liu, Z. G., Wagner, R. 1984. *J. Phys. Paris Colloq.* In press
- von Alvensleben, L., Wagner, R. 1982. See Ref. 27, pp. 563-72
- Miller, M. K., Brenner, S. S., Burke, M. G., Soffa, W. A. 1984. *Scri. Metall.* 18: 111-16
- Zhu, F., Wendt, H., Haasen, P. 1982. *Scri. Metall.* 16: 1175-80
- Zhu, F., Wendt, H., Haasen, P. 1984. See Ref. 29, p. 139
- Brenner, S., Miller, M. K., Soffa, W. A. 1982. *Scri. Metall.* 16: 831
- Zhu, F., von Alvensleben, L., Haasen, P. 1984. *Scri. Metall.* 18: 337

The 1985 Institute of Metals Lecture  
The Metallurgical Society of AIME

## The Early Stages of the Decomposition of Alloys

PETER HAASEN  
R. F. Mehl Medalist

## I. INTRODUCTION

THIS is a report on high resolution microscopy of the formation of a second phase in an alloy. A diffusion controlled reaction is known to occur homogeneously during aging starting from nuclei of radius  $R^* = 2\sigma/\Delta f$ , where  $\sigma$  is the interface energy, of the order 20 mJ/m<sup>2</sup>, and  $\Delta f$ , the gain in free energy on formation of the second phase (per unit volume), typically in the system NiAl) 30 J/cm<sup>3</sup>. Then  $R^* = 15$  Å is the minimum radius of a stable nucleus. For smaller ones more energy is expended in forming the interface than is gained chemically. All of this is well known from the theory of nucleation.<sup>1</sup> The question is how to observe such small particles and to characterize them chemically.

There are, of course, the well established methods of small angle scattering, either of X-rays or of neutrons<sup>2</sup>

The Institute of Metals Lecture was established in 1921, at which time the Institute of Metals Division was the only professional Division within the American Institute of Mining and Metallurgical Engineers. It has been given annually since 1922 by distinguished men from this country and abroad. Beginning in 1973 and thereafter, the person selected to deliver the lecture will be known as the "Institute of Metals Division Lecturer and R. F. Mehl Medalist" for that year.

Dr. HAASEN received his diploma in physics and the Dr. rer. nat. at the University of Göttingen. From 1954-1956 he was a postdoctoral fellow at the Institute for the Study of Metals at the University of Chicago. He was President of the Akademie der Wissenschaften in Göttingen. He held visiting professorships at the Mellon Institute, Pittsburgh, PA, in 1963, at the University of Pennsylvania in 1971, at the University of Paris XIII in 1978, and at Stanford University in 1984. He received the Hevni medal of the Deutsche Gesellschaft für Metallkunde. Since 1959 he has been Professor and Director of the Institut f. Metallphysik at the University of Göttingen, Federal Republic of Germany.

METALLURGICAL TRANSACTIONS A

(SAXS, SANS) which with wave lengths of about 1 Å conveniently resolve particle size and particle spacing (through interference effects). It is very difficult, however, to draw conclusions as to the composition of the particles as a function of aging time, and this is absolutely necessary to differentiate nucleation-and-growth from spinodal decomposition. The final product may be the same in both cases: a periodic array of equilibrium concentration particles, but the reaction path will differ.

Second, there is transmission electron microscopy now able to resolve atoms 3 Å apart (and lattice planes to even smaller spacings). Although, again, there is no analytical capability below the 120 Å range so far, there have been studies of small particles by conventional<sup>3,4,5</sup> and high resolution TEM.<sup>6,7</sup> Figure 1 shows a lattice fringe image of a Ni<sub>3</sub>Al particle precipitated in Ni4 pct Al at 550 °C. The (100) superlattice reflection was used. Smaller particles have too few atoms to produce enough contrast.

The best suited method for resolving small precipitate particles at the moment seems to be field ion microscopy (FIM) combined with time-of-flight (TOF) mass spectrometry, called the atom probe (AP). This instrument will be described in the next section; results on alloy decomposition using the AP will make up the rest of the report.

## II. THE ATOM PROBE

Since E. W. Müller<sup>8</sup> and co-workers published the first design of an AP, several instruments were developed, especially for metallurgical application.<sup>9-11</sup> Currently, only a few instruments are operated in metallurgical laboratories over



Fig. 1—High resolution TEM of NiAl precipitate in Ni41 pct Al aged at 550 °C. Image uses {100} superlattice reflection in particle (S. Möller, Göttingen).

the world but a commercial AP version is on the market now. Figure 2 shows the basic features of an AP designed for our studies (R. Wagner and J. Piller, Göttingen).

Essentially, the instrument consists of two parts: the FIM to image the specimen and the time-of-flight spectrometer, in which single ions, *field evaporated* from the FIM specimen surface are identified. The imaging screen contains in

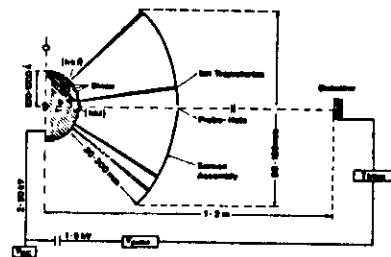


Fig. 2—FIM-atom probe schematically.

its center a probe-hole, through which field evaporated ions, originating from the area covered by the projection of the probe-hole onto the specimen surface enter the flight tube of the atom probe. At the end of the flight tube the ions reach the single-ion detector.

The typical FIM specimen is a sharply pointed needle with a radius of curvature ( $r_t$ ) of about 20 to 80 nm. It is prepared from a thin wire of 0.1 mm to 0.3 mm diameter by anodic electropolishing.<sup>14</sup> All heat treatments necessary for the particular phase transformation have to be performed prior to electropolishing.

After preparation the specimen is introduced into the ultra-high vacuum chamber, ( $\sim 10^{-9}$  mbar) of the FIM, mounted onto a manipulator and cooled to  $\sim 80$  K in order to increase the resolution in the FIM image. The manipulator allows the specimen to be aligned along the axis of the instrument, and any region visible in the FIM image which is to be analyzed with the TOF spectrometer to be shifted until it covers the probe-hole of the atom probe.

The distance ( $R$ ) between tip vertex and the center of the screen can be varied typically between  $\sim 4$  and  $\sim 20$  cm allowing for a variation on the 'average' magnification  $M$  in the FIM.  $M$  is given by

$$\bar{M} = \frac{R}{r_t} \quad [1]$$

With typical values for the mean radius of curvature of the tip ( $r_t$ ) and for  $R$  ( $\sim 3 \times 10^{-6}$  cm and  $\sim 4$  cm, respectively),  $\bar{M}$  is of the order of  $10^6$ . Correspondingly, for the given values the effective diameter ( $d_w$ ) of the AP probe-hole can be varied between  $\sim 3.2$  nm ( $R = 4$  cm) and  $\sim 0.8$  nm ( $R = 20$  cm).

To obtain FIM images from the alloys to which we refer in this article, neon as imaging gas is leaked into the vacuum system ( $\sim 5 \times 10^{-6}$  mbar). Subsequently, a positive high voltage ( $V_{DC}$ ) is applied to the specimen, which typically ranges between 3 and 20 kV depending on  $r_t$ . If the resulting electric field ( $F \sim V_{DC}/r_t$ ) exceeds a critical value ( $F_c \sim 30$  V/nm) the neon atoms are positively ionized in the high field regions above the tip surface and accelerated almost radially toward the grounded FIM screen which lights up at the points of impact.

Starting with a freshly prepared tip the electric field is highest above the sharp protrusions retained from the specimen preparation. As the voltage is gradually increased, the electric field above these protrusions reaches a value  $F_{FE} > F_c$  at which local field evaporation of individual atoms in the form of  $n$ -fold ions ( $n = 1$  and/or 2 for most transition metals) occurs. Since the onset of field evaporation occurs at a certain field strength, regions having smaller radii of curvature field evaporate earlier than those having larger ones.

#### A. Image Formation and Contrast of Decomposed Alloys

The smallest electric field sufficient to ionize the neon atoms is reached only above atoms protruding from the surface. In pure metals these protruding atoms correspond mainly to atoms located in ledge positions at the edges of different stacks of lattice planes. The edges belonging to one stack of {hkl} planes form almost concentric polygons or rings because of the intersection of each stack with the more or less spherically-shaped tip surface. This arrangement of

atoms with localized high-field regions leads to the well-known crystallographic pattern of FIM micrographs of pure metals and dilute alloys.

In most two-phase alloys the precipitates appear either (i) in a bright contrast or (ii) in a dark contrast with respect to the surrounding matrix. In both cases after some field evaporation, a steady state end-form of the FIM tip evolves with the precipitates either protruding from the emitter surface (i) or being blunted (ii) as compared to the local radius of curvature of the adjacent matrix (Figure 3). These local deviations in the radius of curvature above the precipitates are caused by a respectively higher (i) or lower (ii) evaporation field than is necessary in order to field evaporate the surrounding matrix. The contrast of a particular phase may depend also on the image gas and the temperature of the tip. Apparently, the processes of field ionization and field evaporation are highly sensitive to the composition of the precipitates (Figure 4).

Because of the localized change in the radius of curvature above precipitates (Figure 3), a considerable unknown change in the magnification ( $M$ ) of the particular precipitate results. Nevertheless, the size and morphology of visible precipitates can often be determined very accurately without knowing  $M$  by the so-called *persistence-size* technique (Figure 5). By controlled field evaporation several lattice planes of a previously identified pole {hkl} are successively

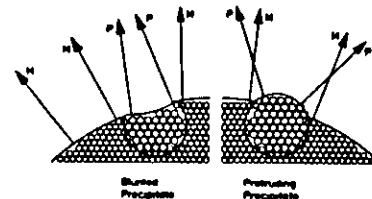
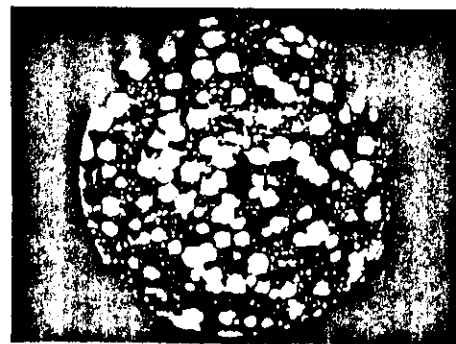


Fig. 3—A precipitate may appear blunted (dark) or protruding (bright) in the tip surface.



Cu-31 Au-2.7Co (at %), 30min 550°C

Fig. 4—Bright precipitates in a decomposed alloy showing individual atoms (H. Wendi, Göttingen).

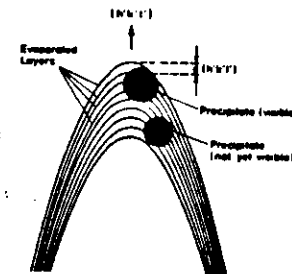


Fig. 5—Field-evaporating layer by layer from the tip; one observes particle morphology.

removed. Whenever a precipitate becomes visible in the vicinity of this pole, the number  $n_{hkl}$  of planes {hkl} is counted which have to be evaporated between the appearance and disappearance of the particle. The dimension of the precipitate along the {hkl} direction is then immediately obtained as  $d(hkl) \cdot n_{hkl}$  with a depth resolution of  $\sim 0.2$  nm. By recording the variations of the intersectional area of the precipitate with the tip surface during the dissection of the precipitate, its morphology can be determined in much detail.

#### B. Atom Probe Analyses

The chemical identification of a single ion is achieved by first measuring its time of flight,  $t$ , and subsequently evaluating its mass-to-charge ratio  $m/n$  (Figure 2). For this purpose, the atoms are field evaporated at a well-defined instant by superposing a high-voltage pulse of a few nanoseconds rise-time to the tip which is held at the imaging voltage  $V_{DC}$  (pulse field evaporation); a pulse width of about 15 nsec and a pulse amplitude  $V_p$  of about 0.15  $V_{DC}$  is found to be appropriate for the analysis of most alloys. Due to the sharp drop of the field strength within a few nm above the tip surface, the field evaporated ions reach their terminal velocity  $v$  shortly after the desorption event and drift with an energy

$$n \cdot e(V_{DC} + V_p) = \frac{1}{2}mv^2 = \frac{1}{2}m \frac{d^2}{t^2} \quad [2]$$

over a distance  $d$  (virtually the tip-to-detector distance; Figure 2) until they strike the ion detector after a time-of-flight  $t$ .

In principle, the quantitative microanalysis of decomposing alloys with the atom probe can be performed in two different ways:

(i) *Selected area analysis* (Figure 5): This type of analysis for the determination of the composition of individual particles is confined to precipitates which are discernible in the FIM image. By rotation of the FIM specimen the particular precipitate is imaged over the probe-hole in the FIM screen. If the effective probe-hole (diameter  $d_w$ ) is larger than the particle,  $d_w$  is decreased by increasing the magnification until the precipitate covers the probe-hole entirely. The composition of the precipitate is now determined by collecting the atoms originating from a cylinder with diameter  $d_w$ , and a length which is limited by the total depth which can be probed before the precipitate has been completely field evaporated. By continuing to probe into the

adjacent matrix and by determining the composition of each successively removed lattice plane, the concentration profile across interphase boundaries can also be obtained. As was discussed in the previous section, in this mode both the size and the detailed morphology can be determined.

(ii) *Random area analysis* (Figure 6): In order to analyze the composition and distribution of particles which are not visible in the FIM or in order to obtain information about solute fluctuations in alloys (e.g., spinodally decomposing alloys), it is necessary to determine the concentration profile in a cylinder of considerable length (e.g., more than 100 nm along a particular direction ( $h'k'l'$ )) with a sufficient depth resolution. For this purpose, the planar concentration of each successively field evaporated ( $h'k'l'$ )-lattice plane is determined and plotted against the number of evaporated planes; hence, the depth resolution is equal to the interplanar spacing  $d(h'k'l')$ . Whenever the analyzed cylinder cuts completely through a particle, its composition and the solute variation across its interphase boundary can be determined directly from the concentration profile. However, if the particle is cut partly by the analyzed cylinder, the concentration profile reveals only a local increase in the solute content as compared to the surrounding matrix ( $c_m$ ) but does not give any information about the true composition of the particle ( $c_p$ ).

By analogy with the analysis of time series, the data contained in an AP composition profile are often analyzed in terms of an autocorrelation analysis, provided the probed distance through the specimen is sufficiently large. This statistical analysis furnishes most decomposition parameters (particularly during the early stages of phase separation where the cluster sizes are small and their number densities large) which are required for a comparison with theoretical predictions (see following section). Figure 7(b) shows the autocorrelation coefficient  $R(k)$  for the concentration profile displayed in Figure 7(a).  $R(k)$  is given by

$$R(k) = \frac{n}{n-k} \frac{\sum_{i=1}^{n-k} (c_i - c_0)(c_{i+k} - c_0)}{\sum_{i=1}^{n-k} (c_i - c_0)^2} \quad [3]$$

$c_i$  is the concentration of the  $i$ -th field evaporated plane ( $h'k'l'$ ),  $c_0$  the mean concentration,  $n$  the total number of field evaporated planes, and  $k$  is the correlation length in units of the interplanar distance  $d(h'k'l')$ . From computer-

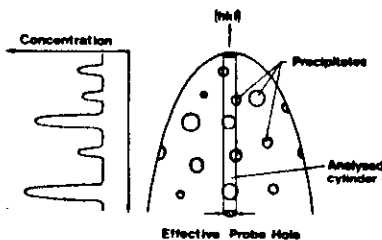


Fig. 6—Random concentration analysis in depth covering a cylinder defined by the projected probe hole.

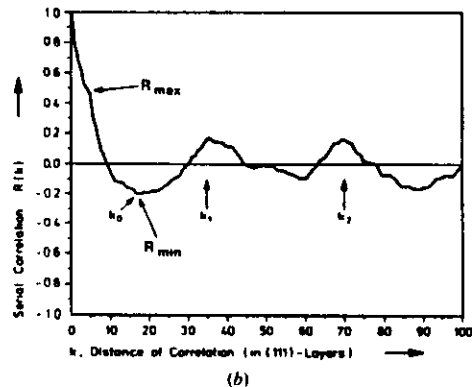
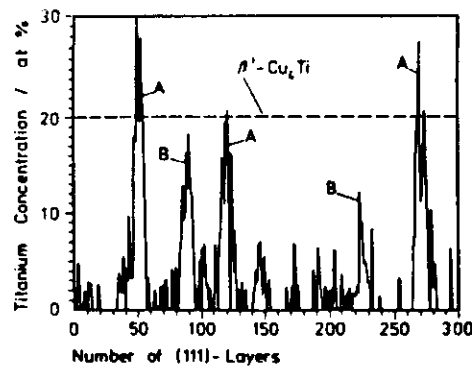


Fig. 7—Concentration profile (a) and correlogram (b) of decomposed Cu-2.7 pct Ti alloy aged 500 min at 350 °C. Particles only partly cut by analyzed cylinder are marked B.  $k_0$ ,  $k_1$ ,  $k_2$  denote particle diameter and spacings, respectively (K. E. Biehl, Göttingen).

simulated atom-probe analyses for which various precipitate microstructures were assumed, it has been established that the parameters  $k_0$ ,  $k_1$ ,  $R_{max}$  and  $R_{min}$  (see Figure 7(b)) are unequivocally related to the mean particle diameter ( $2 \cdot \bar{R}$ ), the interparticle distance ( $\lambda$ ), the particle composition ( $c_p$ ), and the precipitate volume fraction ( $f$ ), respectively.<sup>15</sup> In particular, computer simulations yielded  $\lambda = k_1 \cdot d(h'k'l')$ , and  $2 \cdot \bar{R} = k_0 d(h'k'l')$  for larger particles (e.g.,  $\bar{R} \geq 1.2$  nm); for size distributions with even smaller mean radii, autocorrelation analyses yield  $\bar{R}$  to be somewhat larger than the true values. In Figure 7(b), the occurrence of the second peak at  $k_2$  occurs at exactly twice the distance of the first peak indicating the  $\text{Cu}_3\text{Ti}$  particles to be quasi-periodically distributed. For randomly distributed solute-rich clusters of small number density,  $R(k)$  remains zero for  $k > k_0$ .

The true composition of a solute rich cluster is displayed only in a composition profile if it is covered completely by the probe-hole (see Figure 5); this requires  $d_p < 2 \cdot \bar{R}$ .

Although, in principle,  $d_p$  can be chosen as small as one atomic diameter, reliable statistics require a certain number of atoms to be recorded and, hence,  $d_p$  in the order of  $\sim 2$  nm. Therefore, in most practical cases of analyses of composition fluctuations, the lateral spatial resolution is confined to  $\sim 2$  nm.

It is worth noting that both  $\bar{R}$  and  $\lambda$  can be obtained from autocorrelation analyses regardless of whether the ratio  $d_p/2\bar{R}$  is larger or smaller than unity. Moreover, the Fourier transform of the autocorrelation factor  $R(k)$  yields the (one-dimensional) structure factor  $S(q)$  obtained from scattering experiments ( $q$ : wave vector). Thus, in principle, a random area AP analysis furnishes all the information about the state of decomposition which can be inferred from  $S(q, t)$  as determined in a SAXS or SANS scattering experiment.

### III. NUCLEATION AND GROWTH (NG)

(a) *In the Cu-Co system* wires were homogenized, quenched, aged, thinned, and AP analyzed<sup>16</sup> as described in the previous section. As a particular advantage in this system the precipitated Co-rich particles image brightly in a dark Cu-rich matrix (Figure 4). The diameters of the spherical particles were determined by the persistence size technique, and a size spectrum is shown in Figure 8. Figure 9 shows the dependence of the mean particle radius on the aging time at 550 °C for a Cu-2.7 pct Co and a Cu-2.7 pct Co + 3.1 pct Au alloy. The initial plateau in  $\bar{R}(t)$  is typical for the nucleation also in other systems. The small gold addition evidently accelerated the precipitation kinetics. Figure 10 shows the measured particle density  $N_v$ . The volume fraction precipitated reaches its equilibrium value ( $f_{max} = (4\pi/3)\bar{R}^3 \cdot N_v = 2.75$  pct) within 10 minutes. The particle radius after 1 hour aging at 550 °C did not depend much on the homogenization temperature between 920 and 1020 °C. This shows that the excess vacancy concentration anneals out too quickly (within seconds) to have an appreciable effect on the precipitation kinetics in this system. The composition of several particles was analyzed selectively as shown in Figure 11. Within the scatter the composition after 170 minutes aging at 550 °C (and with a larger scatter also

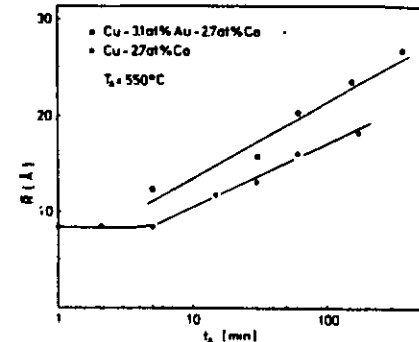


Fig. 9—Mean particle radius vs aging time for two Cu-Co alloys aged at 550 °C (H. Wendt).

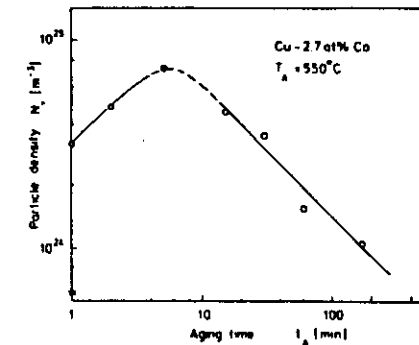


Fig. 10—The particle density grows by nucleation and decreases by coarsening (H. Wendt).

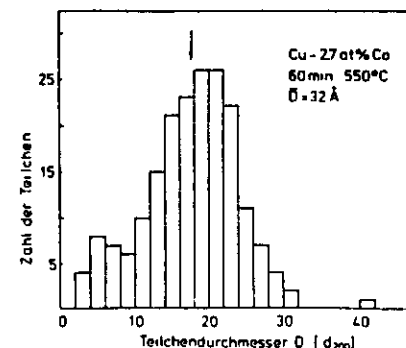


Fig. 8—Particle size spectrum (diameters in units of lattice spacing  $d_{200}$ ) of decomposed alloy (H. Wendt).

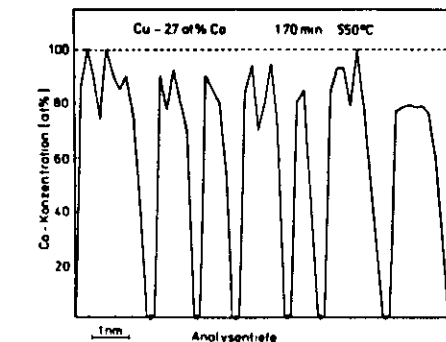


Fig. 11—Cobalt content of individual precipitates focused onto the probe hole and analyzed in depth (H. Wendt).

after 15 minutes) was the equilibrium one, approximately 90 pct Co. The precipitation, therefore, follows the classical nucleation and growth (and not the spinodal) path.

It is interesting to compare this AP study<sup>16</sup> with previous ones: (1) by Servi and Turnbull<sup>17</sup> using electrical resistivity, (2) by LeGoues and Aaronson<sup>18</sup> by using conventional TEM with a resolution of  $\bar{R} = 50$  Å. In (1) alloys with 1 to 2.7 pct Co were investigated aged between 600 °C and 840 °C, in (2) such with 0.5 to 1 pct Co between 460 °C and 620 °C. In (1) only the precipitated volume fraction could be directly inferred; in (2) the number density of  $R \approx 50$  Å particles measured (in the  $N_v$  range  $10^{11}$  to  $10^{13}$  cm<sup>-3</sup> while the AP needs at least  $N_v \approx 10^{17}$  cm<sup>-3</sup> to see enough particles in a tip). Some diffusion-controlled growth was allowed for in calculating nucleation rates from  $N_v$  in Reference 18 but no Ostwald ripening. Concurrent nucleation and ripening (leading to the dissolution of the smaller particles) is an essential feature of the theory<sup>19,20</sup> and the experiments to be reported next.

(b) In the Ni-Al system particles show no FIM contrast: thus a random area and correlation analysis had to be performed.<sup>21,22</sup> An alloy of Ni + 14 pct Al decomposes at 550 °C and forms  $\gamma'$  (Ni<sub>3</sub>Al) precipitates coherently with

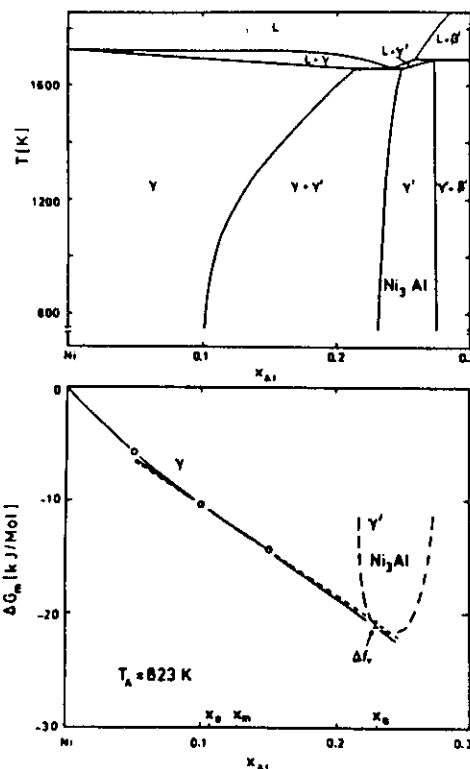


Fig. 12—Phase diagram Ni-Al and free enthalpy of mixing for  $\gamma$  and  $\gamma'$  phases defining the gain in volume free energy on decomposition  $X_m \rightarrow X_0 + X_{Ni_3Al}$ .

the  $\gamma$  (Ni10 pct Al) matrix. Figure 12 shows an evaluation of the existing thermodynamic data to evaluate the gain in volume free energy  $\Delta f_v = \Delta G_p/V_{mat}$  as the matrix composition moves from  $c_m \rightarrow c_0$  ( $\Delta c \rightarrow 0$ ). Figures 13, 14, and 15 give the measured  $\bar{R}$ ,  $N_v$ , and remaining supersaturation  $\Delta c$  as a function of aging time  $t_A$  at 550 °C. An important result is that even the smallest observed precipitates of 10 Å radius or smaller have the equilibrium composition Ni 23 pct Al. This suggests NG and not spinodal character of the process contrary to Reference 23, although it should be noted that at the shortest  $t_A$  the activation barrier  $\Delta F^* = 4 \cdot kT$  is relatively small.

From the long time over-aging kinetics the interfacial energy of the precipitate can be obtained following LSW theory<sup>24,25</sup>

$$\bar{R}^3 - R_0^3 = b t; \quad \Delta c = (\kappa t)^{-1/3} \quad [4]$$

From  $b$  and  $\kappa$  one obtains  $\sigma = 16$  mJ/m<sup>2</sup> and  $D = 10^{-16}$  cm<sup>2</sup> per second. Assuming these quantities to be

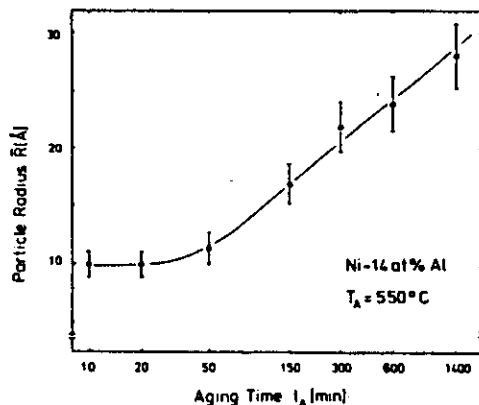


Fig. 13—Mean particle radius vs aging time for Ni14 pct Al.

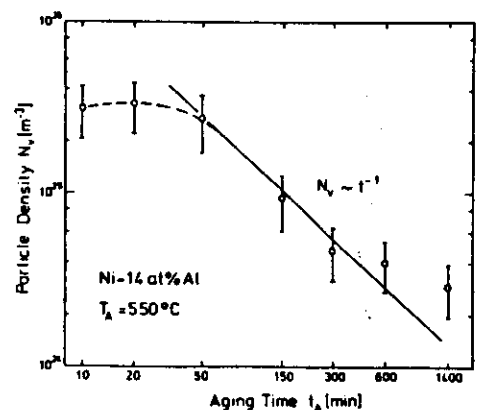


Fig. 14—Same for particle number density.

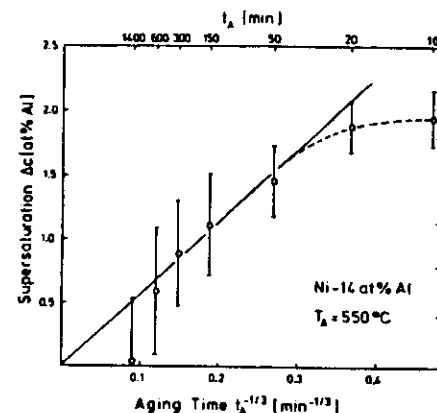


Fig. 15—Same for Al supersaturation  $\Delta c$  and precipitated volume fraction  $f$  (H. Wendi). Time scale (distorted) right to left.

constant during the whole precipitation process, one can now calculate the critical radius of the nuclei  $R^* = 2\sigma/\Delta f_v$  [ $\Delta c(t_A)$ ] from the measured  $\Delta c(t_A)$  (Figure 16(a)). This is compared with the measured mean particle radius in Figure 16(b) and shown to agree rather well. We, therefore, do observe nuclei in the average particles!

For an absolute check of nucleation theory it is necessary to include Ostwald ripening from the very beginning as is seen from the comparison of calculated  $N_v = \int f dt$  with the measured particle density in Figure 17. Here the classical nucleation rate

$$I = N_v u_0 \beta \left( \frac{\delta F^*}{3\pi kT} \right)^{1/2} \exp \left( - \frac{\delta F^* + Q_D}{kT} \right) \quad [5]$$

contains only known quantities:  $\delta F^*$  = nucleation barrier,  $Q_D$  = activation energy of diffusion,  $u_0$  = atomic vibration frequency,  $N_v$  = atom density, and  $\beta$  = ratio of surface to interior atom numbers in  $R^*$ . Langer and Schwarz<sup>19</sup> have proposed a combined nucleation and ripening theory which has been modified to solid-solid transformations<sup>21,22</sup> (MLS model) and numerically integrated without any restrictions by Kampmann and Wagner<sup>23</sup> (N model). The latter authors have fully discussed these theories and their application to our system and to Cu 1.9 pct Ti investigated by v. Alvensleben and Wagner.<sup>23</sup> From Reference 20 Figure 18 is reproduced to show the accuracy of the fit. The following details merit discussion: (a) a nucleation transient is included in Figure 18(b) as a multiple  $c_0$  of the minimum time necessary to diffuse together the extra solute to form the  $R^*$  particle. Experimentally  $c_0 = 3.5$ . (b) During the initial flat part of the measured  $\bar{R}(t)$  nucleation occurs at nearly constant rate from the same nondepleted matrix. (c) Rapid coarsening and dissolution of particles occur already during the bumps in the curves of Figure 18. On the whole the combined NG models describe the experimental situation surprisingly well. Figure 19 shows again the importance of Ostwald ripening determining the half time of the precipitation reaction at high supersaturations, rather than the time for nucleation (the steep part of the curve). In Figure 18(a) there arises the question as to the resolution limit at 10 Å of

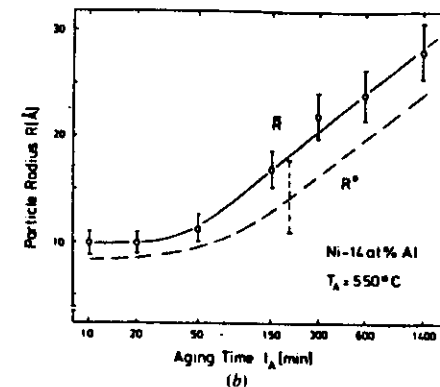
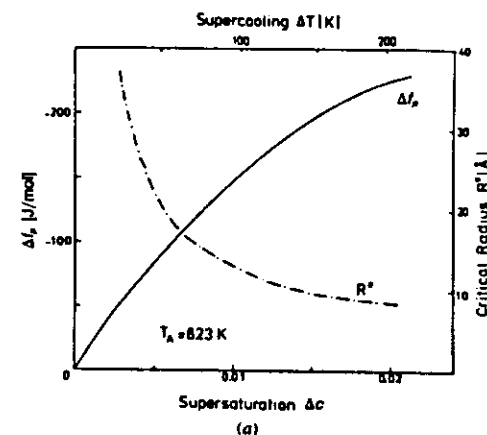


Fig. 16—(a) Critical radius  $R^*$  calculated from  $\Delta f_v$  and  $\sigma$  vs supersaturation is compared with (b) measured mean particle radius  $\bar{R}$  (H. Wendi).

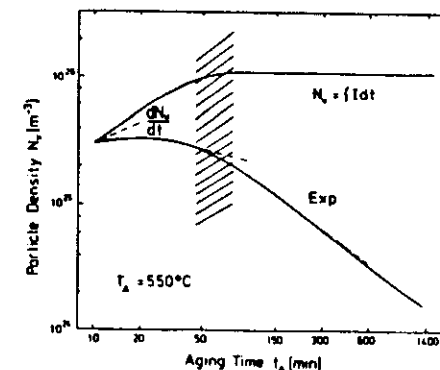


Fig. 17—Density of nucleated particles  $\int f dt$  compared with experimental  $N_v$ . Coarsening occurs already before nucleation period has ended (hatched).

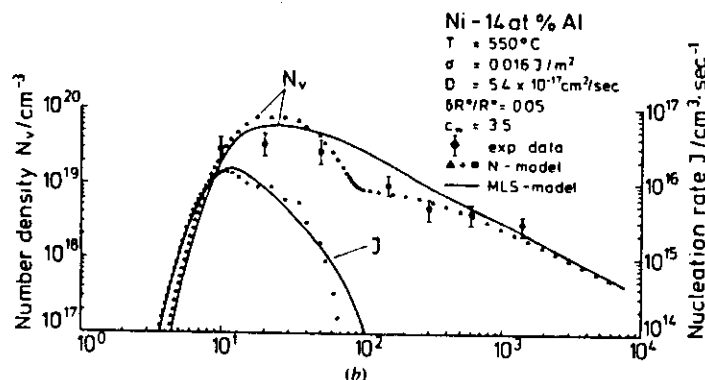
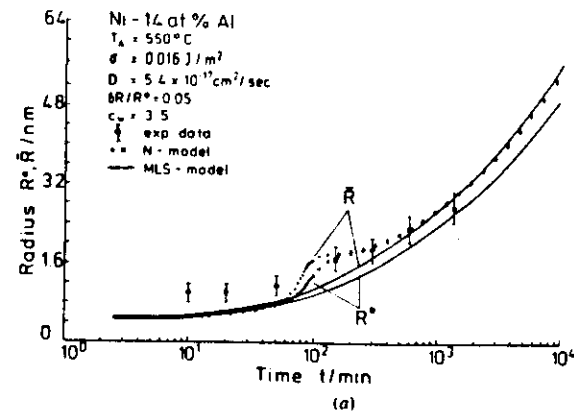


Fig. 18—(a) Calculation of  $R^*$  and  $\bar{R}$  by combined nucleation, growth, and coarsening models of Langer-Schwartz (modified, MLS) and Kampmann-Wagner (N model), see text. (b) Same for particle density and nucleation rate.

the FIM-AP. This might also explain the factor 4 discrepancy between the initial  $R^*$  and  $\bar{R}$  in Cu-Co.<sup>16</sup> In Reference 27 the results of SANS, TEM, and FIM are compared concerning  $\bar{R}(t)$  for Ni (12 to 14) pct Al after aging between 550 °C and 625 °C.

(c) A ternary Ni 36 pct Cu 9 pct Al alloy was investigated<sup>28</sup> to clarify the decomposition mode said to be spinodal<sup>29</sup> as well as the distribution of the third component with respect to the  $\gamma\gamma'$  interface. Again the misfit between the two phases is very small; thus the particles are coherent and coherent. There is, however, welcome FIM contrast between them; see Figure 20.

The particles are found to be of the equilibrium composition  $(\text{Ni}_{40}\text{Cu}_{30})_{10}\text{Al}$  already at the smallest aging time at 580 °C. Thus, the decomposition is by NG. The concentration profile (of Al) across the interface is smooth and very steep (Figure 21) with a width of no more than three lattice planes. This is expected for the relatively low aging temperature. Cu replaces Ni at the interface (Figure 22), but this

may be a nonequilibrium feature at the moving interface as Al diffuses in faster than Cu out. It was not possible to analyze the Al depleted zone expected around a particle because of the small Al content of the matrix. It is interesting in this connection that the LSW analysis at long times yields  $\sigma = 52 \text{ mJ/m}^2$ , much higher than in the binary alloy discussed above.

The measured particle sizes show a distribution that is, at short aging times, 2 to 3 times wider than expected from LSW theory. The mean radius  $\bar{R}(t_A)$  shows a similar time behavior as for the binary alloy (Figure 23). The particles are not randomly distributed but rather regularly with a mean distribution width of ~60 pct of that of a Poisson distribution. The number density  $N_v(t_A)$  is shown in Figure 24 for three aging temperatures. These kinetic data are again evaluated according to the MLS and N-models in Reference 28b. The nucleation barrier is much higher than in the binary,  $\delta F^* = 27 \text{ kJ}$  at 540 °C; the nucleation rate / peaks sharply after several minutes aging to a value of

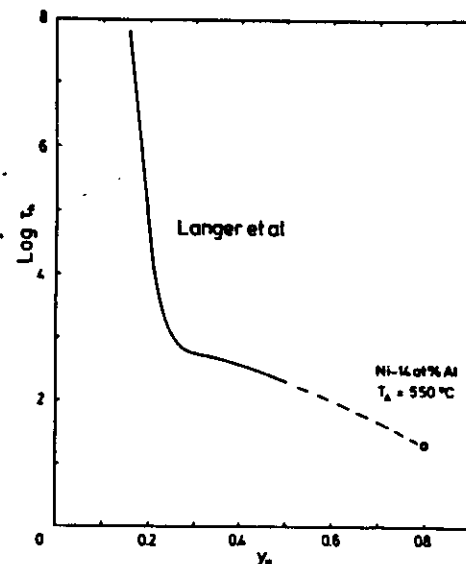


Fig. 19—Half time for precipitation vs (reduced) supersaturation according to MLS-model and experimentally for Ni14 pct Al (H. Wendt).

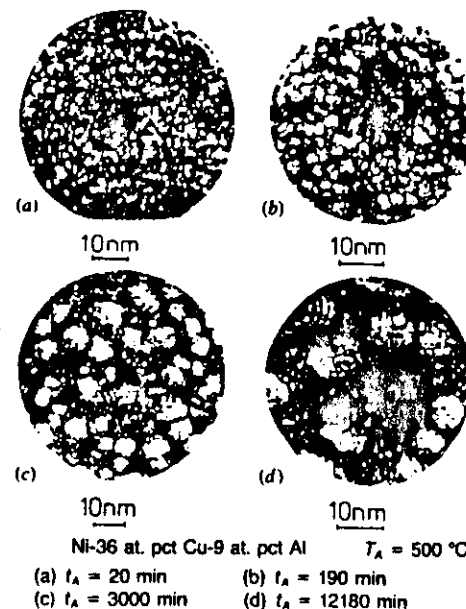


Fig. 20—Growth of precipitates in NiCuAl (Z. Liu, Goettingen).

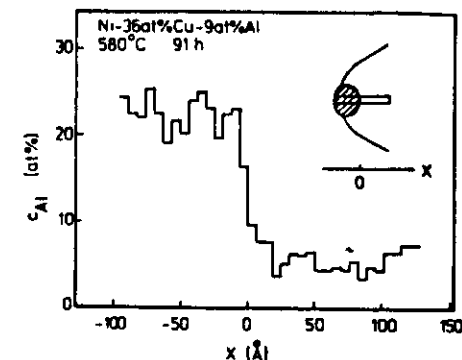


Fig. 21—Al-profile across interface of  $(\text{NiCu})_{10}\text{Al}$  particle (Z. Liu, Goettingen).

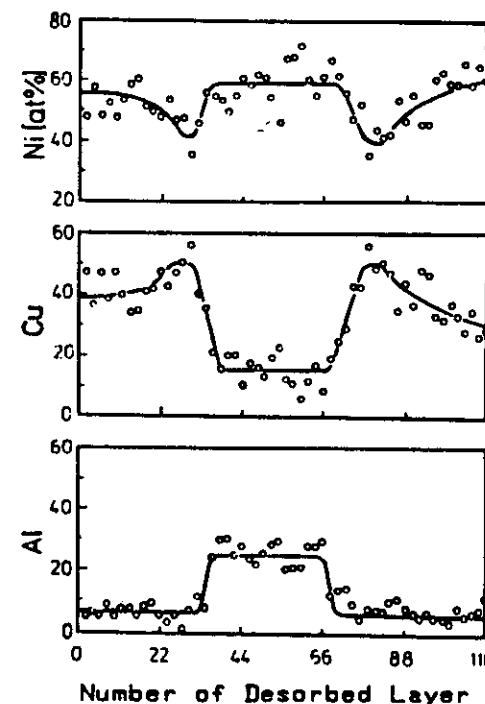


Fig. 22—Enrichment of copper at interface of growing  $(\text{NiCu})_{10}\text{Al}$  particle (Z. Liu).

#### IV. SPINODAL DECOMPOSITION

$10^{17} \text{ cm}^{-3} \text{ s}^{-1}$  after which Ostwald ripening is dominant. Accordingly, the plateaus in Figure 23 are actually longer and at larger  $\bar{R}$  than expected.

A number of binary alloys (Fe 25 pct Be,<sup>30</sup> FeCr,<sup>34</sup> Cu 2.7 pct Ti<sup>31</sup>) and ternary alloys (CuNi (4 to 8) pct Fe,<sup>32</sup> FeCrCu<sup>33</sup>) were studied by FIM and claimed to decompose

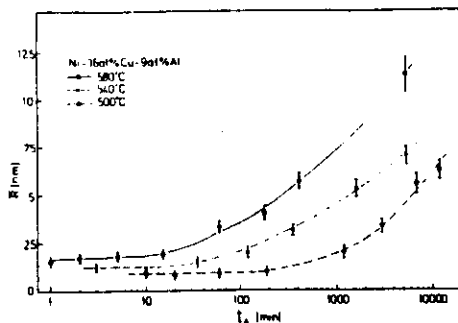


Fig. 23—Kinetics of particle radius  $\bar{R}$  in NiCuAl at various temperatures (Z. Liu).

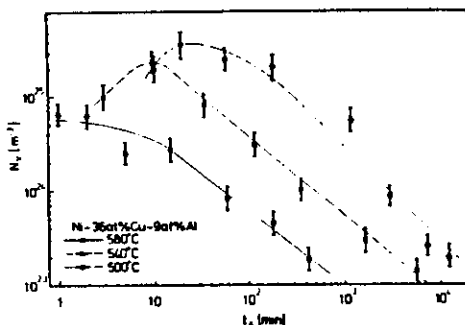


Fig. 24—Kinetics of particle density  $\bar{N}$  in NiCuAl at various temperatures (Z. Liu).

spinodally. FeBe and CuNiFe showed beautiful macro-lattices of the precipitated phases which coarsened by a  $\lambda^2 \sim t$  law in agreement with TEM and SANS measurements. The concentration amplitudes studied in CuNiFe had, however, already reached the final values by the time the precipitates were  $\approx 20$  Å large and could be safely analyzed by the AP. A similar problem occurred in Cu 2.7 pct Ti. Thus, the final proof for the spinodal character of the decomposition, i.e., the time development of the concentration amplitude, is still missing in these cases.

Alloys of Fe 28 wt pct Cr 15 pct Co with minor additions of 1 pct Al, 0.25 pct Zr are useful as ductile magnets (CHROMINDUR). They derive from the FeCr phase diagram which decomposes into two bcc phases called  $\alpha_1$ ,  $\alpha_2$  if the  $\sigma$  phase is suppressed (especially by the Co addition). The Co also extends the miscibility gap to higher temperature and makes it asymmetric toward the Fe side. The aging cycle used in optimum permanent magnet production by Bell Labs (to give the maximum energy product  $(BH)_{max}$ ) is rather complicated and involves aging in a magnetic field just below the Curie temperature (and critical temperature of the gap), i.e., at 625 °C, and further aging at 525 °C to increase the concentration amplitudes. The resulting microstructure of the optimum magnet is shown in Figure 25.<sup>13</sup>

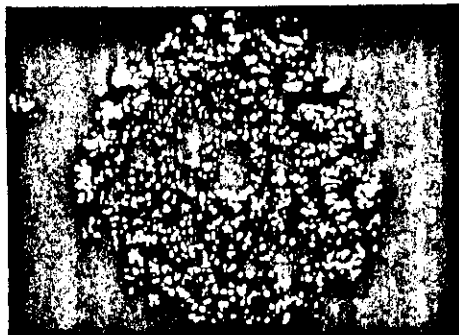


Fig. 25—Two-phase microstructure of optimum FeCrCo magnet (F. Zhu, Göttingen).

The Fe rich phase images brightly, the Cr rich darkly. As one field-evaporates the tip, one follows the contiguity of the two phases in depth: both are sponge-like interconnected and do not resemble iron-rich ellipsoids in a chromium rich matrix as assumed in the elongated-single-domain (ESD) theory of permanent magnets: in this theory the magnetization of a ferromagnetic phase is fixed to the long axis of the ellipsoid isolated from its neighbors by a paramagnetic matrix. This model does not apply also because both phases are ferromagnetic here as could be inferred from AP analyses. Figure 26 gives concentration profiles in depth for Fe, Cr, and Co: the Al seems to follow the iron as does, in fact, the cobalt. It is clearly seen that where Cr enriches, Fe and Co move out. The compositions of  $\alpha_1$  are Fe 6 at. pct Cr 22 pct Co and that of  $\alpha_2$ , Cr 26 pct Fe 6 pct Co. The latter composition is, in fact, weakly ferromagnetic at 300 K with an estimated Curie temperature of 80 °C. The volume fraction of  $\alpha_2$  is 40 pct.

The kinetics of decomposition is followed during aging at 600 °C or 525 °C separately. It is seen in Figure 27 that the Cr concentration amplitude in the dark phase changes slowly with time as expected for SD. The periodicity  $\lambda$  and mean thickness of  $\alpha_2$  regions also increase slowly with the time according to a  $t^{0.24}$  law (Figure 28). This is again in agreement with nonlinear SD theory. It is interesting to note that the decomposition follows the tie line (Figure 29). The dashed line corresponds to an Fe:Co ratio of 3:1.

The morphology of the decomposed alloy with 15 pct Co aged to give 40 pct of the  $\alpha_2$  phase corresponds to the one computer simulated by Cahn<sup>13</sup> for an isotropic spinodal reaction. If the Co content is increased to 24 pct and the aging temperature to 540 °C, the  $\alpha_2$  phase makes up 80 pct of the microstructure and the  $\alpha_1$  phase appears as isolated spheres. Interestingly enough, now the diameter coarsens proportional to  $t^{1/3}$  as expected from LSW theory. The AP analysis for this alloy shows constant composition from  $t \geq 4$  sec on, no longer the slow build-up as for spinodal composition of the 15 pct alloy. It looks as if one has crossed the spinodal as one moved to the side of the miscibility gap with  $\alpha_1$  decreasing from 60 to 20 pct. The morphology changed from interconnected sponge to isolated spheres between  $f_{\alpha_1} = 40 \rightarrow 25$  pct. Another kind of morphology occurred

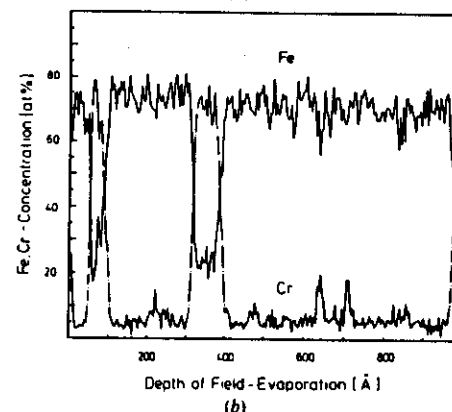
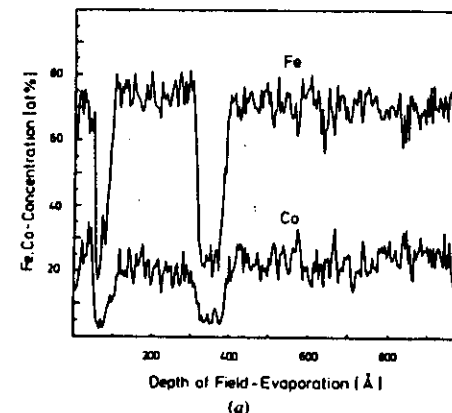


Fig. 26—(a, b) Concentration profiles of decomposed FeCrCo magnet showing Cr rich, Fe/Co poor particles (F. Zhu).

with an alloy of 33 pct Cr, 11.5 pct Co after a complex aging sequence between 670 °C and 500 °C. It showed small bright secondary precipitates in the dark Cr rich phase.

Recently other permanent magnet alloys, the classical Alnicos, were studied.<sup>17,18</sup> Alnico 5 consists of Fe, 8.2 pct Al, 13.6 pct Ni, 26.5 pct Co, 3 pct Cu. (Alnico 8 has 35 pct Co and in addition 5 pct Ti) and was provided for us as cast plates by Thyssen Co. Again, a decomposition of the alloy into two bcc phases ( $\alpha$ ,  $\alpha'$ ) was observed on annealing between 900 °C and 640 °C. The two phases are visible in the FIM as darkly and brightly imaging regions. Three-dimensional field evaporation analysis shows that both phases are contiguous throughout the volume as a sponge-like interconnected network. They are also coherent. The atom probe analysis gives the composition of  $\alpha$  in Alnico 5 as Fe<sub>2</sub>Co, that of  $\alpha'$  as (Ni<sub>10</sub>Fe<sub>4</sub>Al<sub>1</sub>Cu<sub>3</sub>), (in Alnico 8:  $\alpha \approx (\text{Fe Co})$ ,  $\alpha' \approx (\text{Ni}_{10}\text{Co}_{11}\text{Fe}_{11}\text{Al}_{12}\text{Ti}_{11}\text{Cu}_8)$ ). The  $\alpha'$  phase is of the  $\beta'$  (B2) type in the binary NiAl system and should clearly be nonferromagnetic. This still can be reconciled with HVEM observations of "mobile domain walls

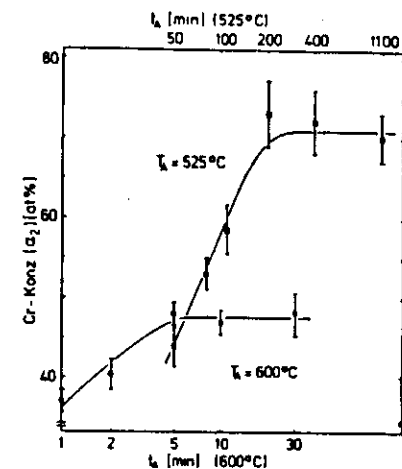


Fig. 27—Slow increase of Cr-concentration in  $\alpha_2$  phase with aging time at two temperatures (F. Zhu).

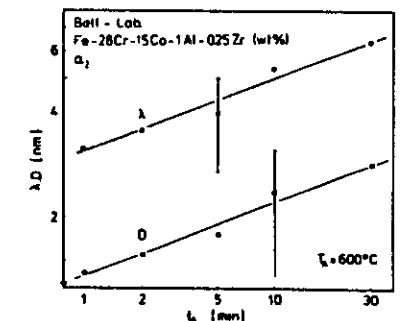


Fig. 28—Growth of spinodal wave length  $\lambda$  and particle diameter  $D$  of  $\alpha_2$  phase on aging (F. Zhu).

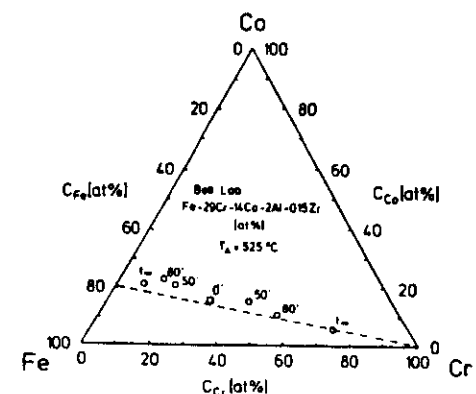


Fig. 29—Connodal path of spinodal decomposition of FeCrCo at various aging times (F. Zhu).



passing through both phases", "though differently from the Chromindurs described above. Indications are found that both phases are at least partly ordered — already at the initial stage of decomposition at 900 °C. The amplitude of the decomposition increases with time, so the process must again be spinodal.  $\alpha$  is the dominant phase in Alnico 5 with a volume fraction of 71 pct (62 pct in Alnico 8). The mechanism of magnetic hardening in the Alnicos (especially after aging in a magnetic field) is likely to be the proposed ESD pinning of the magnetization to the elongated direction of the shape anisotropic  $\alpha$  particles, isolated from each other by the paramagnetic  $\alpha'$  phase. In the Chromindurs, on the other hand, both phases are ferromagnetic, though to different strengths, and continuous Bloch walls are pinned by the softer ( $\alpha_2$ ) phase.

## ACKNOWLEDGMENTS

The author is grateful for the competent work of the Göttingen FIM group built up by R. Wagner and especially to L. v. Alvensleben, H. Wendt, F. Zhu, Z. Liu, and A. Hütten.

## REFERENCES

1. K. C. Russel: in *Phase Transformations*, H. I. Aaronson, ed., ASM, Metals Park, OH, 1970, p. 219.
2. G. Kostorz: in *Physical Metallurgy*, 3rd ed., R. W. Cahn and P. Haasen, eds., North Holland, Amsterdam, 1983, p. 793.
3. D. H. Kirkwood: *Acta Metall.*, 1970, vol. 18, p. 563.
4. R. Gronsky, G. van Tendeloo, and G. Thomas: in *Decomposition of Alloys*, P. Haasen et al., eds., Pergamon, Oxford, 1984, p. 198.
5. F. K. LeGoues: Thesis, Carnegie-Mellon Univ., Pittsburgh, PA, 1983.
6. S. Möller: Diploma Thesis, Göttingen, Germany, 1984.
7. R. Sinclair, R. Gronsky, and G. Thomas: *Acta Metall.*, 1976, vol. 24, p. 789.
8. E. W. Müller, J. A. Panitz, and S. McLane: *Rev. Sci. Instr.*, 1968, vol. 39, p. 83.
9. S. S. Brenner and J. T. McKinney: *Surf. Sci.*, 1970, vol. 23, p. 88.
10. H. O. Andén and H. Nordén: *Scand. J. Metall.*, 1979, vol. 8, p. 147.
11. T. M. Hall, A. Wagner, and D. N. Seidman: *J. Phys. E*, 1977, vol. 10, p. 544.
12. M. K. Miller, P. A. Beaven, and G. D. W. Smith: *Surf. Interf. Anal.*, 1979, vol. 1, p. 149.
13. R. Wagner: *Phys. Blätter*, 1980, vol. 36, p. 65; J. Piller: Dipl. Thesis, Göttingen, Germany, 1977.
14. R. Wagner: in *Crystals*, Springer, Berlin, New York, NY, 1982, vol. 6, p. 1.
15. J. Piller and H. Wendt: *Proc. 29th Intern. FIM Symp.*, Göteborg, 1982, Almquist and Wiksell, Stockholm, p. 265.
16. H. Wendt: Reports to Thyssen Stiftung, 1983, 1984, H. Wendt and P. Haasen: *Scripta Met.*, in press.
17. I. S. Servi and D. Turnbull: *Acta Metall.*, 1966, vol. 14, p. 161.
18. F. K. LeGoues and H. I. Aaronson: *Acta Metall.*, 1984, vol. 32, p. 1855.
19. J. S. Langer and A. J. Schwartz: *Phys. Rev. A*, 1980, vol. 21, p. 948.
20. R. Kampmann and R. Wagner: as Ref. 4, p. 91.
21. H. Wendt and P. Haasen: *Acta Metall.*, 1983, vol. 31, p. 1649.
22. P. Haasen: *Bunsenber. Phys. Chem.*, 1983, vol. 87, p. 201.
23. S. A. Hill and B. Ralph: *Acta Metall.*, 1982, vol. 30, p. 2219.
24. T. M. Lifshitz and V. S. Slyozov: *Phys. Chem. Sol.*, 1961, vol. 19, p. 35.
25. C. Wagner: *Z. Elektr. Chem.*, 1961, vol. 65, p. 581.
26. L. v. Alvensleben and R. Wagner: as Ref. 4, p. 143.
27. R. E. Beddoe, P. Haasen, and G. Kostorz: as Ref. 4, p. 233.
28. Z. G. Liu: *Nachr. Akad. Wissensch.*, Göttingen, 1984, vol. 2, p. 13; Z. G. Liu and R. Wagner: *J. de Phys. Colloq.*, 1984, vol. 45, p. 441.
29. J. Kagawa, T. Miyazaki, and H. Mori: *Trans. JIM*, 1977, vol. 18, p. 707.
30. M. K. Miller, S. S. Brenner, M. G. Burke, and W. A. Soffa: *Scripta Met.*, 1984, vol. 18, p. 111.
31. K. E. Biehl and R. Wagner: *Proc. Int. Conf. on Solid/Solid Phase Transf.*, H. I. Aaronson et al., eds., AIME, Pittsburgh, PA, 1982, p. 185.
32. J. Piller, W. Wagner, H. Wollenberger, and P. Mertens: as Ref. 4, p. 156.
33. F. Zhu, H. Wendt, and P. Haasen: *Scripta Met.*, 1982, vol. 16, p. 1175; as Ref. 4, p. 139; F. Zhu, P. Haasen, and R. Wagner: *Acta Metall.*, in press.
34. W. A. Soffa, S. S. Brenner, and M. K. Miller: as Ref. 4, p. 227.
35. J. W. Cahn: *J. Chem. Phys.*, 1965, vol. 42, p. 93.
36. F. Zhu, L. v. Alvensleben, and P. Haasen: *Scripta Met.*, 1984, vol. 18, p. 337.
37. A. Hütten: Diploma Thesis, Göttingen, Germany, 1985.
38. M. G. Hetherington, J. P. Jakubovics, and G. D. W. Smith: *Proc. of Internat. Field Emission Sympos.*, Paris, France, 1984.

